Aeolian dust accretion outpaces erosion in the formation of Mediterranean alpine soils. New evidence from the periglacial zone of Mount Olympus, Greece

10 authors, including:

Michael Styllas
Institut de Physique du Globe de Paris
60 PUBLICATIONS   **633** CITATIONS

SEE PROFILE

Aurel Persoiu
"Emil Racovita" Institute of Speleology
114 PUBLICATIONS   **2,008** CITATIONS

SEE PROFILE

Athanasios Godelitsas
National and Kapodistrian University of Athens
187 PUBLICATIONS   **2,631** CITATIONS

SEE PROFILE

CASE STUDY

ESPL WILEY

Aeolian dust accretion outpaces erosion in the formation of Mediterranean alpine soils. New evidence from the periglacial zone of Mount Olympus, Greece

Michael Styllas[1] | Christos Pennos[2] | Aurel Persoiu[3,4] |
Athanasios Godelitsas[5] | Lambrini Papadopoulou[6] | Elina Aidona[7] |
Nikolaos Kantiranis[6] | Mihai N. Ducea[8,9] | Matthieu Ghilardi[10] |
Francois Demory[10]

[1]GEOSERVICE LTD, Thessaloniki, Greece

[2]Department of Geography, University of Bergen, Bergen, Norway

[3]Emil Racoviţă Institute of Speleology, Romanian Academy, Cluj-Napoca, Romania

[4]Stable Isotope Laboratory, Ștefan cel Mare University, Suceava, Romania

[5]Department of Geology and Geoenvironment, National and Kapodistrian University of Athens, Zografou Campus, Zografou, Greece

[6]Department of Mineralogy, Petrology and Economic Geology, School of Geology, Aristotle University of Thessaloniki, Thessaloniki, Greece

[7]Department of Geophysics, School of Geology, Aristotle University of Thessaloniki, Thessaloniki, Greece

[8]Faculty of Geology and Geophysics, University of Bucharest, Bucharest, Romania

[9]Department of Geosciences, University of Arizona, Tucson, Arizona, USA

[10]Centre Européen de Recherche et d'Enseignement de Géosciences de l'Environnement (CEREGE)—UMR 7330 CNRS, AMU, IRD, Collège de France, INRAE—Europôle de l'Arbois BP80, CEDEX 04, 13545, Aix-en-Provence, France

Correspondence
Michael Styllas, GEOSERVICE LTD, Eirinis 14 Street, 55236, Thessaloniki, Greece.
Email: mstyllas@gmail.com

Abstract

Soil formation in Mediterranean periglacial karst landscapes remains poorly understood as the interplay between local and allochthonous sources of parent materials, and mineral alteration and pedogenesis, as dominant post-depositional processes, depends on a variety of climatic and environmental factors. Herein, we investigate the balance between erosion and aeolian dust accretion in the formation of an alpine soil profile in the periglacial zone of Mount Olympus in Greece. We applied a wide range of analytical methods to 23 samples, from a soil profile developed in a glaciokarstic plateau, from colluvial sediment horizons interbedded in postglacial scree slopes of different maturity and formation age and from modern Sahara dust samples deposited on the snowpack. Colluvial sediment horizons exhibit high concentrations of carbonate gravel and calcite-rich sand and represent the local erosion products. The soil B horizon developed on the glaciokarstic plateau, contains high amounts of fine earth and is rich in quartz, mica, plagioclase, clays and Fe–Ti oxides. Based on physical and textural characteristics, the soil profile is partitioned in a surficial weathered Bw and an illuvial Bt horizon that overlies the local regolith composed of fragmented glacial till and slope wash deposits. Radiogenic isotope systematics, textural and mineralogical analysis show that the contribution of aeolian (Sahara and locally sourced) dust to the development of the soil B horizon ranges between 50% and 65%. Cryoturbation results in fine earth translocation from Bw to the Bt horizon, whereas weak pedogenetic modifications of detrital (aeolian and bedrock-derived) minerals result in magnetic mineral weathering and secondary clay formation. Our findings reveal that aeolian dust accretion from Saharan and lcal sources is the dominant process in providing alpine soil parent material and that cryoturbation, weak pedogenesis and clay mineral alteration occur within the Mediterranean periglacial zone of Mount Olympus.

KEYWORDS

aeolian dust accretion; alpine soil; erosion; Mediterranean periglacial zone, Mount Olympus, Greece; mineral weathering

1 | INTRODUCTION

Global glacier retreat and the melting of permafrost have altered the dynamics of the alpine critical zone by enhancing erosion and by disturbing the production of mountain soils (Egli et al., 2014; Haeberli et al., 2006). During periods of glacial retreat and paraglacial adjustment, alpine soils develop from parent materials sourced through a combination of frost shattering, colluvial activity and hillslope outwash (Egli & Poulenard, 2016). An equally important factor that affects the formation and evolution of alpine soils is the accretion of local and long-range transported aeolian dust (Drewnik et al., 2014; Gild et al., 2018; Küfmann, 2008; Lawrence et al., 2013; Muhs & Benedict, 2006; Munroe et al., 2019; Yang et al., 2016). Thus, the contributions of physical erosion and aeolian dust accretion are fundamental sources of alpine soils' parent material and largely define their textural, mineralogical and geochemical characteristics.

The postglacial adjustment of alpine valleys is inherently linked to high rates of erosion, with frequent rockfalls, debris flows and rock avalanches and to high rates of sediment production particularly below their steep rock walls. In such dynamic environments, alpine soil mantles formed on the surface of slope deposits are patchy, often truncated and constantly rejuvenated by rockfall material and snowpack movements, whereas the evolution of these soils alternates between progressive and regressive phases (Egli et al., 2018). Similar soil mantles developed on fine gravel and sandy layers deposited on the surface of stratified scree slopes are indicative of quiescent periods of slope processes and are thus concise indicators of optimum climatic conditions and alpine landscape stability (Sanders et al., 2010). When the regional climate shifts to a colder regime, intense freeze–thaw activity and frost cracking enhance rockfall activity and result in the erosion and gradual burial of these incipient soil mantles. As hillslope processes and scree slope aggradation diminish away from the alpine steep rockwalls, the development of alpine soils on distal moraines, outwash plains and glacially scoured plateaus can be considered continuous (sensu lato). In these depositional environments, low erosional rates provide ample time for pedogenetic processes such as chemical weathering, mineral alteration, elemental translocation and illuviation to occur, whereas periglacial processes, such as cryoturbation disturb the soil profiles. Alpine soils are an important component of high mountain ecosystems, so a better understanding of the processes that drive their formation in climatically sensitive regions such as the Mediterranean is required.

Most soils formed in the Mediterranean basin display a distinguishable red color (terra rossa) that derives from high concentrations of ultra-fine pedogenic iron oxides, mainly hematite (Durn et al., 1999; Yaalon, 1997). Terra rossa soils receive significant aeolian dust additions from the Sahara and Sahel regions (Durn, 2003; Stuut et al., 2009; Yaalon, 1997). Aeolian dust accretion in terra rossa soils can also originate from a wide range of alluvial deposits, such as sand dunes, desiccated alluvial planes and Quaternary loess (Amit et al., 2020; Erel & Torrent, 2010; Lehmkuhl et al., 2020), especially during cold and arid periods of sea level lowstands and subsequent continental shelves' exposure (e.g., Razum et al., 2023). In the Mediterranean alpine hinterland, thin drapes of Sahara dust-rich soils are found on glacial plateaus, moraines and outwash plains (e.g., Rellini et al., 2009), but also on non-glacial karst plateaus (e.g.,D'Amico et al., 2023). Most of the Mediterranean mountains are built up by

carbonate rocks; hence, the aeolian input to alpine soil formation occurs in parallel with colluvial deposition of carbonate erosion and dissolution products that form a characteristic insoluble residue incorporated in the soil sequences (Durn, 2003; Kirsten & Heinrich, 2022; Varga et al., 2016).

In the present study, we investigate the major processes that drive the postglacial formation of Mediterranean alpine soils in the periglacial landscapes of Mount Olympus, Greece. We follow a combined sedimentological, mineralogical and isotopic approach and present a detailed characterization of distinct alpine sediment and soil horizons developed across a geomorphological gradient of decreasing erosive power. Discrete sediment samples from intact sandy layers interbedded in postglacial stratified scree slope deposits that represent the in situ erosional products are compared with samples from a soil profile developed in a glaciokarstic plateau, with a goal to assess the relative contributions of aeolian dust accretion to the fine fraction of the alpine soil. We compare their respective grain size distributions, bulk mineralogy and elemental composition in order to differentiate between the physical and chemical processes that drive the deposition of the sandy layers and the production of the scree slope incipient soil horizons and of the glaciokarstic plateau alpine soil profile. Furthermore, we examine the potential influence of Sahara and locally sourced aeolian dust accretion on the alpine soil through the application of grain size modes contributions, mineralogical compositions and $^{86}Sr/^{87}Sr$ and $^{143}Nd/^{144}Nd$ ratios between the soil samples and Sahara dust samples collected from the snowpack. We finally measured the magnetic properties of the soil samples and analysed the clay mineralogy of the bottom and topsoil layers, to assess the potential weathering of iron oxides and secondary formation of clay minerals within the Mount Olympus periglacial zone. Understanding the sources of parent materials and soil formation processes between contrasting geomorphological settings is a fundamental step towards defining the postglacial paleo-environmental history of Mount Olympus alpine landscapes that followed pronounced shifts in the regional climate.

2 | BACKGROUND

2.1 | Mount Olympus' glacial history

Mount Olympus is the highest mountain in Greece, rising 2918 m above the northwest coastline of the Aegean Sea (Figure 1a). It is a precipitous massif with a circular shape composed of Triassic to Cretaceous metacarbonates, uplifted along a frontal fault that runs parallel to the present-day shoreline. Mount Olympus is exhumed from the silicate crystalline bedrock, which dominates the lithology of Pieria Mountains (granites and ophiolites) to the north and east, and Mount Olympus granites to the west (Figure 1b). High uplift rates along with successive Quaternary glaciations have created the present-day rugged terrain. The deglaciation of Mount Olympus since the Last Glacial Maximum (LGM), between 28 and 24 ka BP (Allard et al., 2020), triggered the rapid retreat of an ice cap that covered the summit area and extended down to elevations of ~1800 m (Kuhlemann et al., 2008). The post-LGM glacier retreat was intercepted by two glacier readvance phases at ~15 and at ~12.5 ka BP that were limited in the highest cirques above 2200 m (Styllas et al., 2018). This latter phase
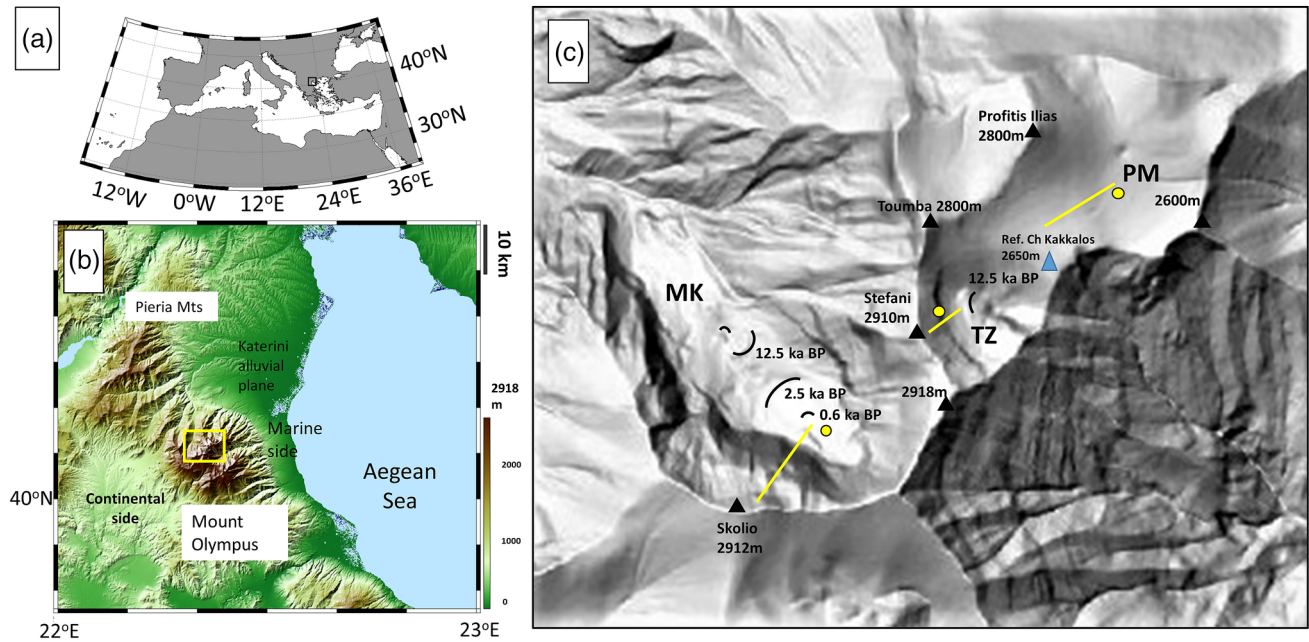
FIGURE 1 (a) General setting of the study area within the Mediterranean basin. (b) Mount Olympus alpine domain (yellow box), with the two respective piedmonts on the marine and continental sides, where Mount Olympus granites outcrop, the silicate bed-rock Pieria Mountains and the Katerini alluvial plane (SRTM 90 digital elevation model). (c) The highest cirques and plateau of Mount Olympus with the respective locations of dated moraines (black curved lines from Styllas et al., 2018), the sampling locations considered in this study (yellow circles) and the geomorphological transects described in Figure 2 (yellow lines). MK, Megala Kazania cirque; TZ, Throne of Zeus cirque; PM, Plateau of Muses.

of glacial expanse is traced both in the Megala Kazania (MK) and Throne of Zeus (TZ) cirques (Figure 1c). The absence of absolutely dated glacial features between early- and late-Holocene (9–3 ka BP) in both cirques suggests reduced glacial activity, whereas late Holocene (3 ka BP to present) glacier advances have been observed only in the MK cirque (Figure 1c). These include a terminal moraine stabilization phase at ~2.5 ka BP followed by a smaller expansion of the MK glacier at the beginning of the Little Ice Age (LIA) at ~0.6 ka BP (Styllas, 2020). Late Holocene glacier advances in the MK cirque lack similarly dated glacial landforms in the TZ cirque, but we cannot rule out the possibility that the Late Holocene climatic shifts towards glacial conditions triggered an intensification of glacial and periglacial processes, which in turn affected the late Holocene landscape evolution, and resultant scree slope aggradation and alpine soil production.

2.2 | Climate

The contemporary maritime conditions and the steep relief of Mount Olympus result in intense precipitation and temperature altitudinal gradients, with the highest peaks constituting an orographic and climatic barrier between the eastern (marine) and western (continental) sides (Figure 1b, Styllas & Kaskaoutis, 2018). The climate in the coastal zone is typically Mediterranean, whereas at higher elevations (1000–2200 m), the climate attains sub-Mediterranean characteristics with average annual precipitation of 1300 mm (Styllas et al., 2016). In the alpine zone above the tree line (2400 m), the climate is characterized by temperate conditions with annual precipitation above 2000 mm and average annual temperatures between 0 and 1.5°C (Styllas et al., 2016). The periglacial activity in the Mount Olympus

alpine zone is likely still active today, as it is situated just above the lower limit of the regional permafrost zone (2700 m) of the southern Balkan peninsula (Dobiński, 2005).

2.3 | The Plateau of Muses

The Plateau of Muses (PM) is a planar depositional surface located at an elevation of 2600 m with a surface area of 1 km². It resembles a typical alpine meadow, partly covered by alpine grass vegetation and shares similar characteristics with plateaus found in the high Balkan Mountains and in the European Alps. The PM is bounded to the south by the TZ cirque lateral moraine ridge and by several gently sloping glacially eroded peaks along its northern, eastern and western margins (Figure 1c). The formation of the plateau has resulted from the combined action of glacial scouring and carbonate bedrock dissolution. Its low relief in combination with the circular shape suggests a doline-type karstic depression that is filled with glacial till, overlain by slope wash sediments transported from the catchment slopes. The surface layer of the PM sedimentary sequence comprises a soil sequence with variable thickness (30–50 cm) that overlies a layer of outwash sand and fine gravels and/or fragmented till boulders and exhibits brown-red to yellow color hues, which in the Munsell color scale range between 7.5 and 10 YR (Table 1). Alternating patches of alpine grass vegetation and hummocky soil pans in the centre of the plateau are indicative of periglacial activity and cryoturbation. Other periglacial features such as solifluction-terraced stripes below the bare bedrock of the surrounding summits are tentatively considered to have formed during the Late Holocene cold stages, during the observed expansion of small glaciers in the MK cirque.

TABLE 1 Physical characteristics of the soil samples retrieved from the interbedded colluvial soils of the Megala Kazania (MK) and Throne of Zeus (TZ) scree slopes and from the alpine soil formed on the Plateau of Muses (PM).

Sample ID	Depth below surface(cm)	Munsell color (dry)	Clay (%)M1 (<2 μm)	Fine silt(%)M2 (3.5–5 μm)	Silt(%)M3 (14–30 μm)	Fine sand (%)M4 (65–110 μm)	Coarse sand (%)M5 (300–800 μm)
MK1	30	5Y 6/1	1.7	6.6	0.0	39.8	51.9
MK2	250	5Y 6/1	0.0	11.4	0.0	47.5	41.1
TZ1	50	2.5Y 5/4	5.3	10.0	0.0	67.9	16.8
TZ2	150	10YR 3/4	6.0	25.2	0.0	43.5	25.3
TZ3	120	10YR 3/4	5.8	18.2	0.0	56.9	19.1
PM1	0–2	7.5YR 3/6	7.8	12.7	76.5	0.0	3.0
PM2	2–4	7.5YR 3/6	9.8	14.7	74.5	0.0	1.0
PM3	4–6	7.5YR 3/6	8.5	13.4	76.9	0.0	1.2
PM4	6–8	7.5YR 3/6	8.0	12.6	78.2	0.0	1.2
PM5	8–10	7.5YR 3/6	9.8	16.1	72.5	0.0	1.6
PM6	10–12	7.5YR 2/4	9.3	15.7	73.8	0.0	1.2
PM7	12–14	7.5YR 3/6	9.3	15.7	73.8	0.0	1.2
PM8	14–16	10YR 3/4	13.0	23.3	61.3	0.0	2.4
PM9	16–18	10YR 3/4	13.8	24.2	60.1	0.0	1.9
PM10	18–20	10YR 2/4	14.5	25.2	58.8	0.0	1.5
PM11	20–22	10YR 3/4	14.0	24.5	60.2	0.0	1.3
PM12	22–24	10YR 3/6	14.6	25.1	58.6	0.0	1.7
PM13	24–26	10YR 3/6	16.3	27.5	55.0	0.0	1.2
PM14	26–28	10YR 3/4	16.0	28.5	52.1	0.0	3.4
PM15	28–30	10YR 4/6	16.2	28.6	52.6	0.0	2.6
PM16	30–32	2.5YR 5/6	15.6	28.5	50.8	0.0	5.1

3 | MATERIALS AND METHODS

3.1 | Erosional products and alpine soil sampling

To adequately address the relative contributions of aeolian dust accretion and local erosion of moraines and scree slopes to the development of the alpine soil on Mount Olympus periglacial zone, we used a wide range of methods that involved the analyses of 21 discrete soil and sediment samples retrieved along a transect of decreasing hillslope energy and erosional power (Figure 2). Five samples were retrieved from clast-free sandy horizons interbedded in the relatively young (Late Holocene) MK and older (early Holocene) TZ stratified scree slopes, and 16 were sampled from the PM soil sequence at 2-cm intervals (Table 1). The specific experimental setting was selected to evaluate the impact of physical weathering on providing the base material for the development of the PM soil. We only sampled naturally exposed clast-free sandy layers found within the scree slopes of MK and TZ. We considered that these layers share similar textural, mineralogical and geochemical characteristics with the PM soil basal horizon, which lies on a layer of outwash sand and gravel. Luckily, we were able to retrieve the samples from two distinct interbedded clast-free sediment layers within the TZ scree slope, after a torrential rainfall event that opened a deep erosional trench in the scree slope below the rock wall and reached the basal till layer (Figure 2 middle row central photo). The scree slope in the MK is regularly eroded and scoured from a perennial snowfield that is retreating by the end of the summer season, and this made the sampling of distinct soil-sediment horizons straightforward (Figure 2 middle row left photo). We manually excavated only one pit for high-resolution soil sampling and considered that due to the very small surface area of the surficial soil apron within the PM catchment (0.06 km²), the specific profile is representative of the PM soil development. We selected a location in the centre of a circular soil-sediment pan that was free of vegetation and surface carbonate fragments (Figure 2). After sampling, the pit was closed and refilled with the excavated material in accordance with Mount Olympus National Park directions. In locations with long-lasting snowpacks, we observed a humic A horizon, but since these locations host several endemic flower species, the Management Unit of Mount Olympus National Park did not grant permission to excavate a soil pit in these sensitive sites. The PM soil samples were additionally subjected to microscopic and radiogenic isotope analyses and magnetic measurements to investigate the potential chemical alteration processes during soil development. Mineralogical and radiogenic isotope analyses were also performed in two samples of aeolian dust that were deposited on the PM snowpack during the spring seasons of 2018 and 2022. The long-range aeolian dust transport episodes occurred on March 22–24, 2018, and March 16–18, 2022. The synoptic conditions of these distinct episodes show that the dust emissions travelled to Mount Olympus from the Sahara Desert and left an orange hue on the snowpack, which later in the spring season formed distinct layers in the snowpack (Figure 3). We therefore consider the samples collected from the PM snowpack as representative of Sahara dust accretion in Mount Olympus alpine soils.
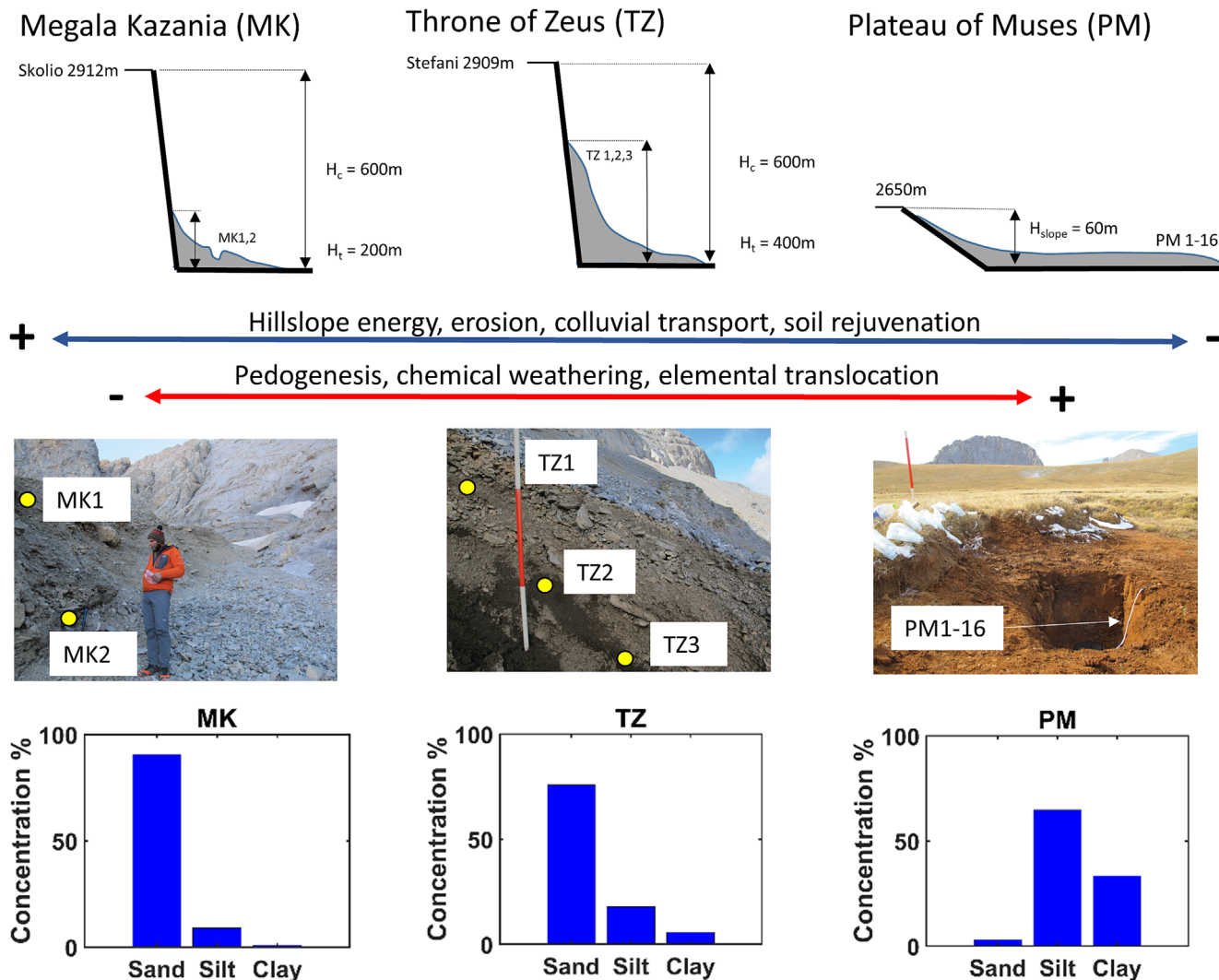
FIGURE 2 Conceptual diagram of the study, with the sampling sites, the morphological profiles shown in Figure 1c as yellow lines, and with their respective textural characteristics that resulted from grain size analysis. The respective heights of the rock cliffs (H_c) and talus slopes (H_t) are also shown. The soil samples from the stratified scree clast-free horizons in MK cirque are located behind the Little Ice Age moraine (left upper panel, photo and diagram). The stratified scree slope under the rock wall of Stefani (2910 m) in the TZ cirque, with the respective locations of the clast-free soil samples (centre panel, photo and diagram) and the soil profile in the PM (right panel, photo and diagram).

3.2 | Grain size analyses

The soil samples were wet sieved through a 3.5-mm sieve and treated with 30% hydrogen peroxide (H_2O_2) at 70°C for 12 h to remove organic matter. H_2O_2 treatment was repeated three times until the samples were completely bleached and all organic matter was degraded. The samples were washed with distilled water and analysed with a Mastersizer 3000 laser diffraction particle size analyser to define the bulk grain size distributions of the sand, silt and clay fractions, respectively. The samples were run through an automated dispersion unit and sodium hexametaphosphate solution (Calgon) was added as the dispersion factor. Statistical analyses of the grain size distributions and derivation of the clay, silt, and sand fractions were realised with MATLAB Curve Fitting Lab (CFLab), which performs curve fitting on sediment grain size

distributions using the Weibull probability distribution function (Wu et al., 2020).

3.3 | Mineralogy

Identification of the mineral phases of the soil and aeolian dust bulk samples was achieved through X-ray diffraction (XRD, Philips diffractometer PW1800, Co radiation at 40 kV and 40 mA) on all samples. Two additional samples from the top and base of the PM soil profile (PM1 and PM15) were additionally analysed for their clay (<2 μm) mineralogy through ethylene glycolation and heating for 2 h at 550°C. The PM soil samples' semi-quantitative composition of the main mineral phases (e.g., quartz, feldspar, plagioclase, micas and calcite) was determined using MAUD-Material Analysis software applied for full
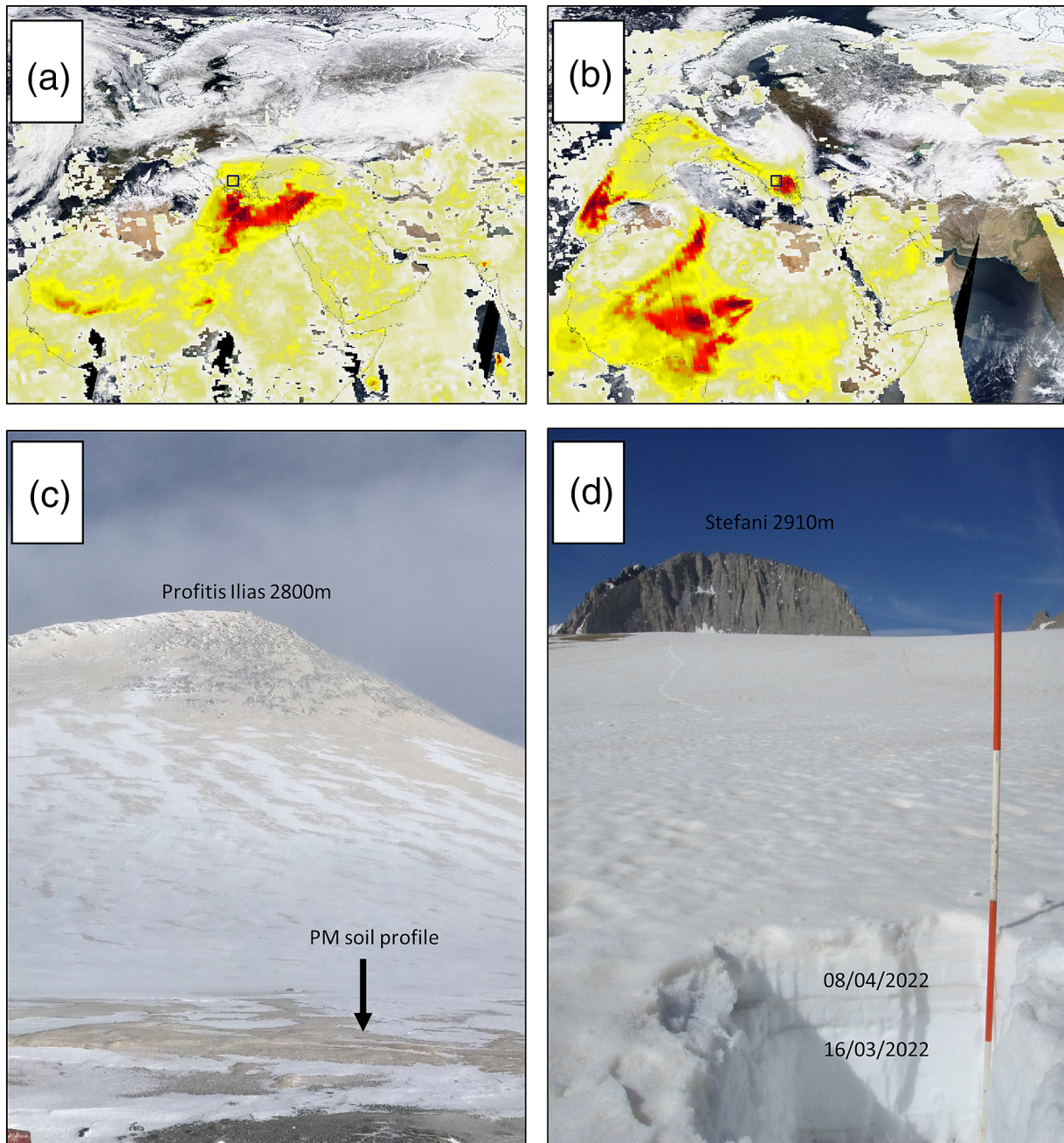
FIGURE 3 Synoptic maps and direct observations of two Sahara dust episodes on Mount Olympus alpine critical zone (black rectangle). Aerosol optical depth (AOD) during March 22, 2018, (a), and March 16, 2022, (b), events showing the trajectory of dust plumes from the Sahara Desert, and their impacts on the snowpack of the Plateau of Muses (c, d). The PM soil profile is indicated by the black arrow (c), whereas the snow pit (d) with successive Sahara dust transport episodes in the springs of 2018 and 2022 has been excavated on top of the PM soil profile. The NASA SUOMI/NNP aerosol optical depth composition product was downloaded from the NASA EOSDIS Worldview platform (worldview. earthdata.nasa.gov).

pattern Rietveld refinement (Lutterotti et al., 2007) and is expressed as weight percent (wt%) concentrations.

3.4 | Petrographic, magnetic and isotopic analyses

Additional analytical methods were applied only to the PM soil samples to assess the relative sources of soil-forming material, and the potential for pedogenesis, and chemical weathering. The fabric configuration of the PM alpine soil was explored through scanning electron microscopy–energy dispersive spectrometry (SEM–EDS) analyses

(JEOL JSM-840A equipped with an INCA 250; Oxford) with a 20-kV accelerating voltage and 0.4-mA probe current. Backscattered electron images (BSEs) enabled us to detect the shapes of different minerals, and physical weathering features of specific grains, whereas with the EDS analysis, we examined areas of different chemical composition within the same soil aggregates.

We additionally explored the existence of ferromagnetic components and the potential for iron oxide weathering and secondary formation in the PM soil profile through measurements of magnetic susceptibility. The discrete samples were packed in cubical plastic boxes ($2 \times 2 \times 2$ cm) and weighed before the measurements.

Volume-specific magnetic susceptibility measurements were performed using a Bartington dual MS2B sensor at low and high frequencies of 0.465 and 4.65 kHz. The results are expressed as mass-specific magnetic susceptibility (χ; 10^{-8} m^3 kg^{-1}). Every sample was measured three times, and the average value was assigned as the final measurement. For each sample, two air measurements were performed before and after sample measurement. The frequency-dependent susceptibility (χ_{FD}; %) was calculated according to Dearing et al. (1996):

$$\chi FD\% = \frac{100(\chi LF - \chi HF)}{\chi LF} \qquad (1)$$

where χ_{LF} and χ_{HF} are the magnetic susceptibility at low and high frequencies, respectively. Samples PM16 and PM15, which were considered more representative of the PM soil regolith boundary, were additionally subjected to thermomagnetic analysis to define the origin of the ferromagnetic particles at the base of the PM soil. Measurements of continuous thermomagnetic curves (K–T curves) at low and high temperatures were realised with the furnace CS3 of the AGICO MFK1-FA susceptibilimeter.

The potential sources of the PM soil and aeolian dust were evaluated through their Sr and Nd isotopic ratios. Isotopic measurements were performed at the University of Arizona TIMS laboratory following the procedure in Conroy et al. (2013) for soil samples. Samples were not spiked and dissolved in mixtures of ultrapure Hf-HNO3 acid. Elemental separation of dissolved samples was carried out in chromatographic columns via HCl elution in a clean laboratory environment. Conventional cation columns filled with AG50W-X4 resin were used for Sr and REEs separation and anion columns with LN Spec resin for Nd separation following Ducea et al. (2020). Sr cuts were loaded onto Ta single filaments and Nd cuts onto Re filaments. ^{87}Sr/^{86}Sr and ^{143}Nd/^{144}Nd ratios (Table 3) were measured on a VG Sector 54 thermal ionization mass spectrometer (TIMS) fitted with adjustable 1011 Ω Faraday collectors and Daly photomultipliers. NBS SRM 987 Sr standard and La Jolla Nd standard were analysed during the sample run to ensure the performance of the instrument and to perform some minor corrections on the final reported ratios.

3.5 | Erosional potential and aeolian dust accretion proxies

The erosional potential of the three sampling sites equally distanced along a 2-km transect was derived from field estimates of the vertical height of the MK and TZ rocky headwalls and their deposited scree slopes. We evaluated the plateau and scree slope energy distribution and maturity stage from the dimensionless ratio between the vertical height of the scree slope (Ht) to the vertical height of the headwall (Hc) following Statham (1976) (Figure 2).

To assess the potential contribution of distal and local aeolian dust inputs in the PM soil we used the quartz weight percent concentrations (wt.%). The source of aeolian quartz can be local, from the Pieria Mountains silicate bedrock and from the granites to the west of Mount Olympus, or can be transported during Sahara dust episodes. The quartz depicted from XRD analyses of the PM snowpack samples is in line with Sahara dust samples from the Pyrenees, the European Alps and the Carpathian Mountains that contain quartz rich samples (e.g., Rellini

et al., 2009; Rodriguez-Navarro et al., 2018; Marmureanu et al., 2019). Herein, we cannot exclude the possibility of quartz release from the local bedrock through periglacial erosion and carbonate dissolution, but the amount of quartz released from local bedrock dissolution is expected to be small, as the wt.% concentration of the insoluble residue from carbonates in Greece is less than 1% (Kantiranis, 2001; Kirsten & Heinrich, 2022; MacLeod, 1980). In addition, the grain size distribution and δ^{18}O values of quartz grains from soil profiles developed on Cretaceous limestones in central and western Greece suggest an aeolian (Saharan-derived and locally derived) origin (Mizota et al., 1988). Therefore, it is reasonable to consider quartz (wt.%) as a reliable proxy of aeolian dust accretion on Mount Olympus.

We selected the ε_{Nd} ratio as a second independent proxy of Sahara dust accretion in the PM soil. We did not use the Sr ratio (^{87}Sr/^{86}Sr) as it can be impacted by the dissolution of carbonate particles and replacement of Ca by Sr during carbonate weathering and pedogenetic alteration of the PM soil (e.g., Shalev et al., 2013). Sr isotopic distributions of PM soil can be further complicated by the accretion of sea-salt-derived Sr through orographic precipitation (Kurtz et al., 2001). Rain is not a significant source of Nd, so the addition of rainwater and snow should not affect the Nd isotopic composition of the aeolian dust, as ε_{Nd} is buffered against these changes (Kurtz et al., 2001). We estimated the fraction of Sahara dust from the ε_{Nd} ratios of the PM soil, the dust deposited on the snowpack, and the local bedrock following the method by Kurtz et al. (2001):

$$f = \frac{(\varepsilon Nd\,PM\,soil - \varepsilon Nd\,bedrock)}{(\varepsilon Nd\,Sahara\,dust - \varepsilon Nd\,bedrock)}. \qquad (2)$$

As we had not obtained direct Sr and ε_{Nd} values from Mount Olympus bedrock, we used the value of basal sample PM16, which is dominated by bedrock-derived calcite and falls in the same value range with basin-average values of terrestrial, coastal and marine sediments deposited in the Aegean Sea (e.g., Weldeab et al., 2002).

4 | RESULTS

4.1 | Alpine soil formation across a hillslope energy gradient

According to Statham (1976), Ht/Hc values above 0.4 characterise a mature scree slope, which is the case for the TZ (0.6) but not for the MK (0.3) scree slope, and this reflects the older deglaciation age of the TZ cirque (~12.5 ka BP, Section 2.1). The MK scree slope is deposited behind the LIA moraine (Figure 1c), so that the most recent deglaciation processes (~0.6 ka BP to present) have resulted in immature scree development. Conversely, the low-relief, low-erosion PM acts as a long-term depocentre of slope wash and detrital (aeolian and bedrock derived through freeze–thaw action) sediments. For this low-energy setting, we believe that minor colluvial contributions, cryoturbation, aeolian dust accretion, fine earth translocation and post-depositional mineral alteration are the major drivers of PM soil production. The irregular boundary between the base of the PM soil and the underlying regolith composed of glacial till and outwash gravels, is indicative of cryoturbation, whereas observations of late-season soil freezing and waterlogging (Figure 4) provide permissive

evidence that PM soil development is disturbed by cryogenic processes. The energy gradient along the contrasting environments impacts the soil color. The PM soil basal layer overlying the regolith shares similar color characteristics with the MK samples and with the TZ upper sediment horizon, which have grey to olive green hues (Munsell dry color 2.5–5 Y; Table 1). Conversely, the lower clast-free sediment horizon of the TZ scree shares similar Munsell dry color characteristics with the PM soil, characterised by red-brown to yellow hues (7.5–10 YR, Table 1), suggesting that these soil samples are more oxidised and are undergoing pedogenetic alterations.

4.2 | Grain size variation

The interactions between slope processes, colluvial sediment transport, and aeolian sub-additions result in polymodal grain size distributions that display different shapes among MK and TZ sediment horizons and PM soil. Five grain size modes (M1 to M5) were mathematically derived from the application of the CFLab curve-fitting algorithm. Fitting degrees were >99% and fitting residuals were <0.1%, indicating excellent fits for the raw grain size distribution curves (Figure 5a–d). The fine-earth (clay and silt) fractions resemble grain size modes M1 and M2 with respective mean grain sizes of ~2 and ~4 μm and M3 with mean grain sizes between 10 and 30 μm. The sand fraction is composed of two modal sub-populations: a fine-sand-grain size mode (M4, mean grain size ~80 μm) and a coarse sand-grain size mode (M5, mean grain size 440 μm) (Figure 5e–h; Table 1). Coarse sand is transported to the respective interbedded sediment horizons by rockfall activity and colluvial processes, or in the case of the low-sloping PM, through slope wash processes. The fine sand (M4) subpopulation was not traced in the PM soil samples, and this can be linked to either selective entrainment of M4, or to distortion of the MK and TZ grain size curves and truncation of the coarser modes (Garzanti et al., 2009).

In addition to the distinct color variations, the contrasting slope-energy distribution between the MK, TZ scree slopes and the PM depositional environments defines their textural compositions.

Sediment horizons developed on the surface of the MK scree slope contain higher amounts of sand (~90%) and lower amounts of silt and clay (~10%) compared with their TZ counterparts (~75% and ~25%), implying that the dominance of sand in the sediment horizons of the scree slopes derives from freeze–thaw and colluvial activity. The coarse-sand content (M5) of the PM soil basal layer is 6% but is lower within the solum (2%–3%), suggesting either reduced periglacial activity and/or low transport capacity of erosional products from the catchment through slope wash processes (Table 1; Figure 2, lower graphs).

The grain size distribution curves of the PM soil present a significant change in shape between soil depths of 14 and 16 cm, which is characterised by a 15% reduction of the clay and very-fine-silt fractions (M1 and M2) and by a similar increase of silt contents (Figure 5a,b). This sharp textural differentiation was not supported by field observations, where the solum appeared homogenous without distinct pedogenetic horizons and without any visual evidence of an erosional layer (Figure 6a), but it is supported by changes in the soil color. The samples above a soil depth of 14–16 cm exhibit red to brown hues (7.5 YR), whereas the samples below this layer have more yellow-red (10 YR) hues (Table 1). We also observed clay coatings in sparse secondary carbonates (calcretes) along the lower part of the PM soil profile, which we interpret as evidence of soil mixing, downward translocation of dissolved Ca and secondary calcite precipitation at the base of the soil profile. Based on these observations, we partitioned the PM soil profile into two horizons: an upper Bw horizon between 0 and 14 cm with red to brown hues, low clay (~25%) and high silt (~75%) contents, and a lower illuvial Bt horizon between 14 and 32 cm with higher (~40%) clay contents, a yellow-red hue, and higher amounts (~5%) of sand compared with the overlying Bw horizon (Figure 6).

4.3 | Soil and aeolian dust mineralogy

The XRD analysis of the bulk samples reveals a mineralogy that substantially differs between the MK, TZ and PM soils and, like the soil
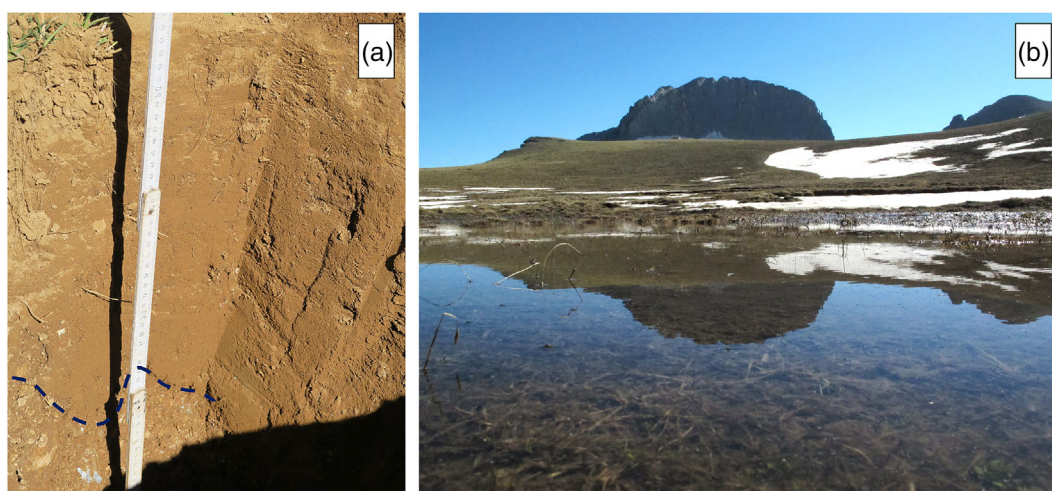

FIGURE 4 Evidence of soil disturbance on the Plateau of Muses under past and present-day climatic conditions. (a) An irregular gravel layer (blue dashed line) between outwash gravels and the overlying soil resulting from cryoturbation. (b) Early summer season freeze of the soil surface layer and subsequent waterlogging (photo taken on June 2012).

FIGURE 5 Cumulative grain size distributions of the soil samples from MK and TZ and from PM soil Bw and Bt horizons (a–d). Surface sample PM1 (a, blue line) shows a distinct grain size distribution from the PM soil upper layer. Subplots e–h: results of the CFLab fitting algorithm with the respective sample grain size distributions (red curves) and mathematically deduced grain size modes M1 to M5 (blue curves) of soil samples PM1, PM15, TZ1 and MK2, representing distinct soil sub-populations.
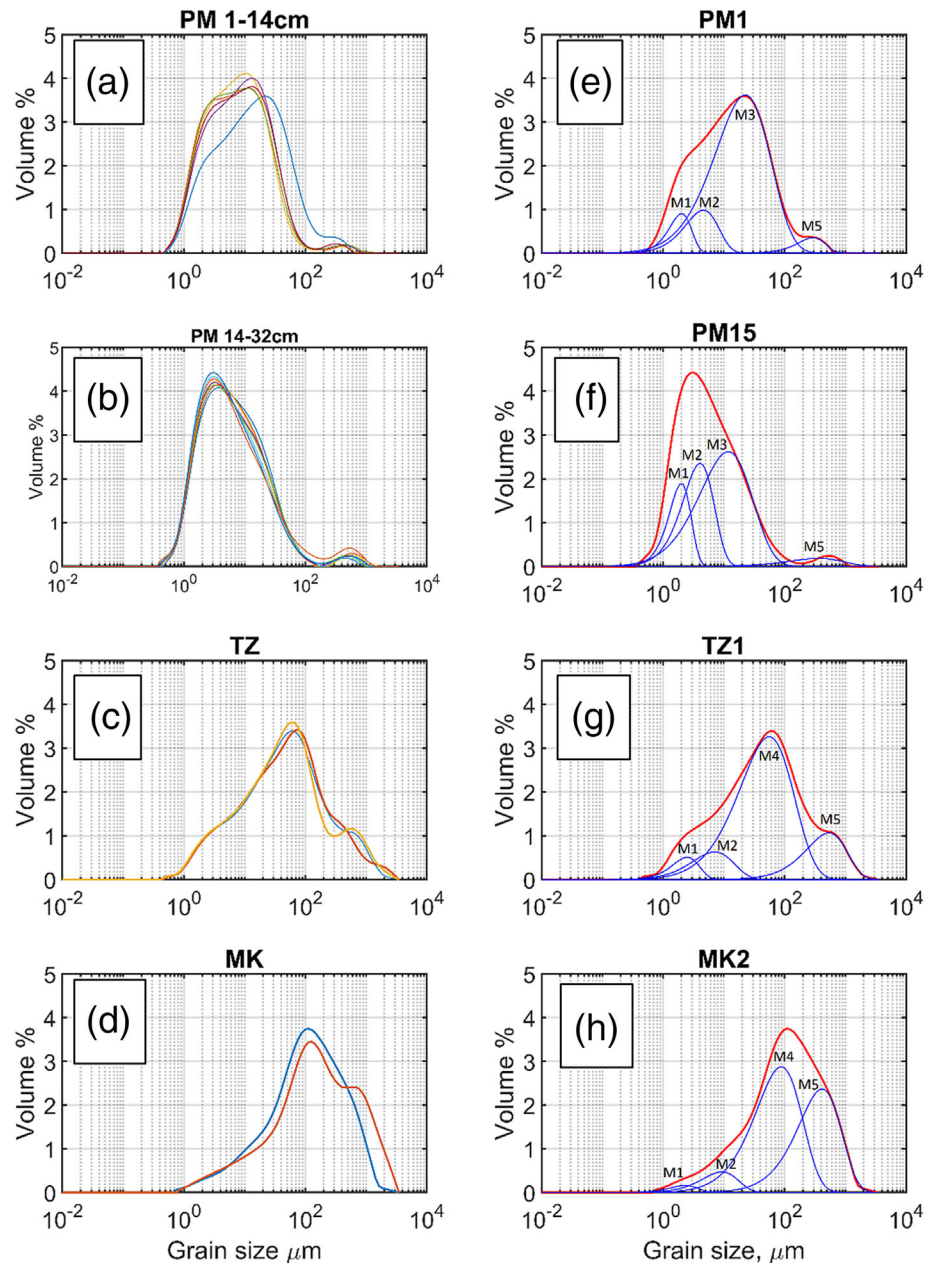
colorization and grain size variations, follows the erosional slope gradient. The most dominant mineral phase in the clast-free material of the MK and TZ soils is calcite. Other minerals identified include dolomite, quartz and micas. Conversely, the bulk mineralogical composition of PM soil exhibits a richer suite of minerals that includes quartz, chlorite and mixed layer clays, mica, potassium feldspars and plagioclase (Figure 7). Calcite is dominant (~50%) only in basal sample PM16 (Figure 6; Table 2). Quartz, clays, and mica are the most dominant mineral phases in the PM soil (~90%) with low values in basal sample PM16 (50%), whereas plagioclase and potassium feldspars represent the remaining 10% (Table 2). Semi-quantitative analysis of the clay mineralogy of two samples retrieved from the surface of the Bw horizon and the base of the Bt horizon (samples PM1 and PM15) revealed high concentrations of smectite and kaolinite (80%) and low contents of chlorite and illite. Surface sample PM1 contains 45% smectite and 35% kaolinite, whereas basal sample PM15 has higher smectite (65%) and lower kaolinite (25%) contents (Table 2).

From the comparison of the XRD spectra (Figure 7), it is obvious that the bulk mineralogy of the PM soil matches that of the Sahara dust samples. Both Sahara dust samples show the presence of clay minerals, quartz, mica, calcite, plagioclase, K-feldspar and dolomite. The detected mineral phases are typical of Saharan dust deposited in Europe during both dry- and wet-deposition events (Scheuvens et al., 2013). Additionally, recent studies of Saharan dust wet deposition in the Iberian Peninsula also indicated the presence of Fe–Ti oxides, such as goethite and hematite, and of Ti oxides, such as rutile (Rodriguez-Navarro et al., 2018), but these minerals were not depicted from our XRD analyses. Despite their overall XRD spectral similarity, a pronounced difference between the contemporary Sahara dust and PM soil samples is the presence of calcite and dolomite in the dust samples and their near absence from the PM soil profile (Figure 7). The smooth and low-intensity peaks for calcite and dolomite at 29.43 and 30.7 2θ in surface sample PM1 indicate the partial removal of calcite and dolomite, whereas similarly subdued peaks in basal sample PM16 denote near complete decalcification of the solum (Figure 7).

4.4 | Magnetic susceptibility of PM soil

The magnetic susceptibilities of the PM soil bulk samples were measured to provide insight into the ferromagnetic components of the PM soil and their potential alterations. Overall, the low-frequency magnetic susceptibility (χ_{lf}) is higher in the lower Bt horizon, with average values for samples PM8–PM16 of 55×10^{-8} m^3 kg^{-1}, and lower χ_{lf} values in the surface Bw horizon, with average values for samples PM1–PM7 of 36×10^{-8} m^3 kg^{-1} (Figure 8a). Similar value ranges were measured for the high-frequency magnetic susceptibility (χ_{hf}). The estimated values of frequency-dependent (χ_{FD}) susceptibility range between 0% and 14%, with significantly higher values in the surface Bw horizon (Figure 8b). High χ_{FD} values (>10%) are indicative of the presence of superparamagnetic Fe oxide nanoparticles (<0.05 μm, Dearing 1999), suggesting a higher amount of detrital (aeolian and/or bedrock-derived), or secondary ultrafine ferrimagnetic grains in the surface horizon Bw. The depth variation of bulk samples χ_{lf} follows that of the clay fraction (Figure 6b), whereas the χ_{FD} that of the silt fraction (Figure 6c).

The mineral phases responsible for the bulk magnetic enhancement of the Bt horizon were deduced from high-temperature magnetic susceptibility measurements performed during a single heating–cooling cycle to 700°C (Figure 8c). We estimated the Curie temperature (T_c) of samples PM16 and PM15 to examine the potential existence of superparamagnetic particles in the base of the PM soil profile, which is in contact with the regolith. The thermomagnetic analysis of sample PM16 failed completely, likely due to its high calcite content and to the absence of high amounts of magnetic phases. On the other hand, sample PM15 within the soil–regolith lower boundary, revealed a uniform χ–T behavior that is indicative of the dominance of two magnetic phases (Figure 8c)—one with Tc, or transformation temperature, between 260 and 320°C, representing likely maghemite, and a second one around 600°C, which is typical for oxidised magnetite (Jordanova et al., 2022). Since the nano-sized pedogenic magnetite is unstable upon heating (Dunlop & Özdemir, 1997), the identified oxidised magnetite suggests that weak pedogenetic production of ferromagnetic components occurs in the base of the PM soil profile.

4.5 | Radiogenic isotopes

More information on the provenance of the PM-soil-forming material was derived from the radiogenic isotope analysis of the soil samples and of the Sahara dust samples. The ^{87}Sr/^{86}Sr values of PM soil samples range from 0.71437 to 0.72071 and the ε_{Nd} values from −7.75 to −9.80 (Table 3). Overall, the PM soil ^{87}Sr/^{86}Sr−ε_{ND} cluster together apart from sample PM16, which has the lowest ^{87}Sr/^{86}Sr value (Figure 9). The analysed Sahara dust sample exhibits an ^{87}Sr/^{86}Sr value of 0.71272 that falls within the lower range of North African dust sources between ~0.71200 and 0.74000 (Erel & Torrent, 2010; Grousset & Biscaye, 2005). The Sr isotopic ratio of the Sahara dust sample shows potential mixing with rainwater and local sea salt aerosols during the March 2018 wet deposition event but also with other European aerosol sources, which is validated by the fact that the dust plume of March 2018 travelled over Europe before it reached Mount Olympus (Figure 3a). The Sahara dust sample has an ε_{Nd} value of −6.80. Plotting the ^{87}Sr/^{86}Sr and ε_{Nd} measurements against literature values from terrigenous, coastal and marine sediments from the Aegean Sea region (Weldeab et al., 2002) reveals an isotopic similarity between the Sahara dust and PM16 samples with these sediments (Figure 9). A reasonable interpretation of this observation comes from the fact that basal sample PM16 resembles the soil regolith and plots close to the contemporary and Holocene values of Aegean Sea terrestrial, coastal and marine sediments that likely represent a mix of Sahara dust with Cenozoic bedrock carbonates, which are overall characterised by low ^{87}Sr/^{86}Sr values of <0.70800 (Capo et al., 1998; Frank et al., 2021). The two subclusters of PM soil samples have more radiogenic values compared with those of the rest of the samples and clearly correspond to Bw and Bt horizons. The increasing silt content towards the surface of the PM soil profile (Figure 6c, Table 1) occur with changes of the ^{87}Sr/^{86}Sr and ε_{Nd} values towards more crustal values (color variation in Figure 9) that are representative of the central Sahara province. Therefore, the increases in silt fraction within the PM soil profile can be directly linked to increases in Sahara dust accretion. Increased Sahara dust accretion is
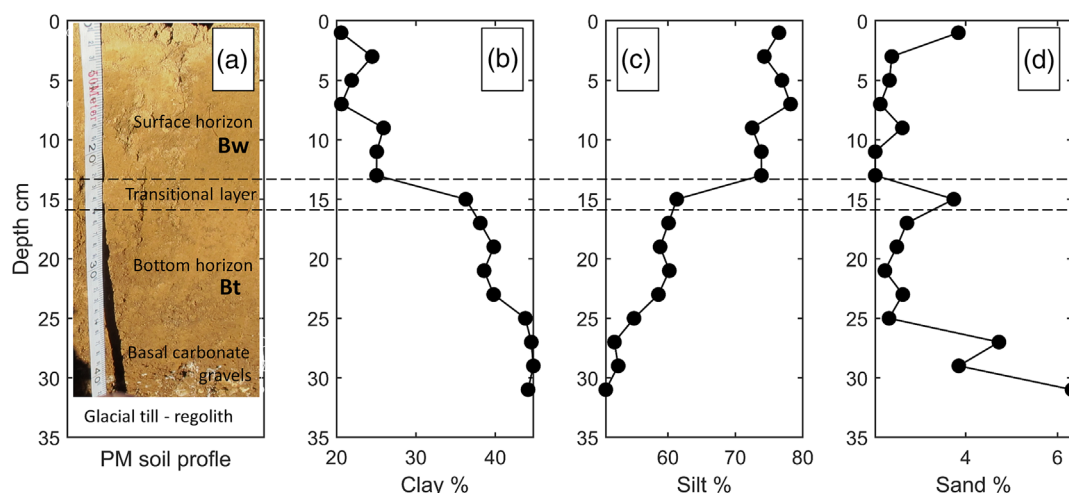

FIGURE 6 Photo of the PM soil profile and depth variations of the main textural classes. A transition layer between 14 and 16 cm of soil depth marks a substantial decrease in clay and an increase in silt contents and a change in the dry soil color. For clarity reasons, it is noted that the direct depth measurement of the PM soil begins at 10 cm along the measurement tape, explaining the discrepancy between the actual and the illustrated depth. The photo was taken 1 day after the profile excavation, when the upper part had partly dried out.

FIGURE 7 X-ray diffraction (XRD) patterns of soil samples PM1, PM15, TZ1 and MK2. Soils within the high-energy scree deposits are composed primarily of calcite. In contrast, PM soil samples contain quartz, clays, feldspars and mica (M, mica; Chl/M, chlorite and mixed layer clays, likely smectite; Chl/K, chlorite and likely kaolinite; K, K feldspar; Qz, quartz; Pl, plagioclase feldspars; Cc, calcite; Dol, dolomite).
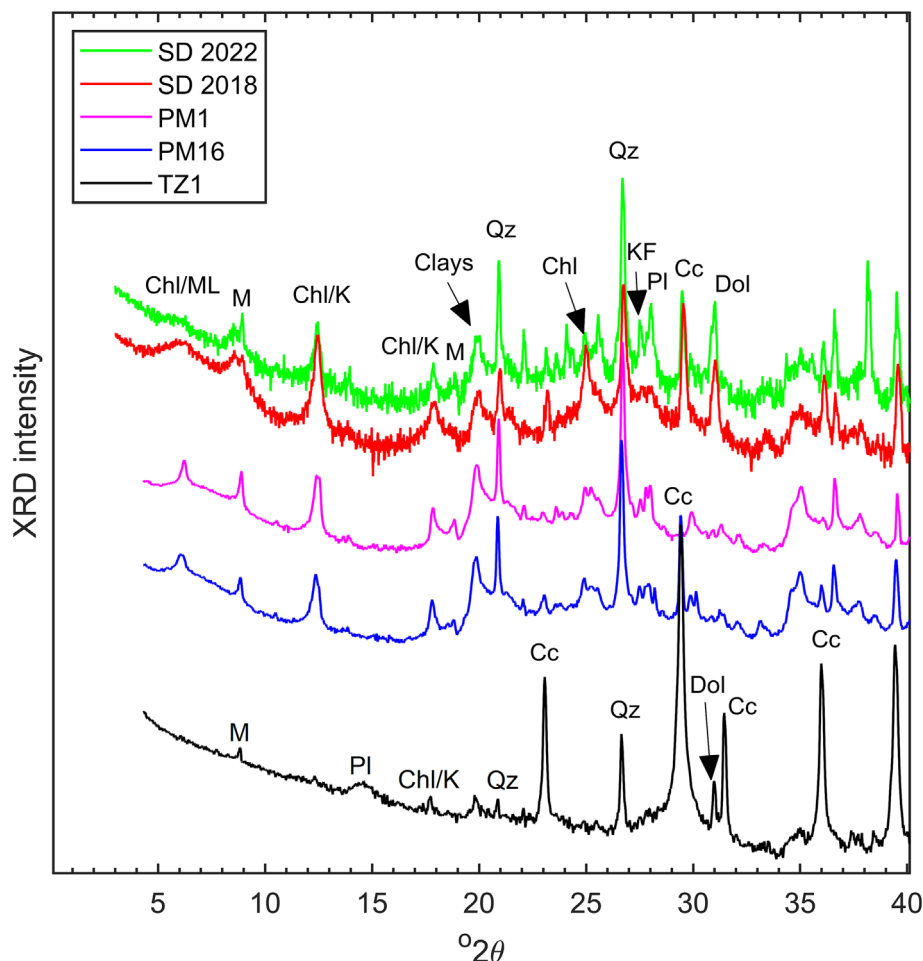
TABLE 2 Weight percent (wt%) mineralogical semi-quantitative composition of the PM soil, along with the clay mineralogy of surface and base samples PM1 and PM15.

Sample ID	Qtz	Chl_CC	Plag	KF	Mica	Amph	Cc	Clay mineralogy (<2 μm) Sm/Kaol/Chl/Ill
PM1	55	21	14	3	7	0	0	Smectite: 45%, Kaolinite: 35%, Chlorite: 10%, Illite:10%
PM2	59	26	6	1	8	0	0	
PM3	66	21	4	2	7	0	0	
PM4	52	31	7	3	7	0	0	
PM5	64	22	7	0	7	0	0	
PM6	60	24	7	2	7	0	0	
PM7	62	20	4	6	8	0	0	
PM8	59	24	7	3	7	0	0	
PM9	61	24	7	3	5	0	0	
PM10	64	22	8	1	5	0	0	
PM11	58	28	4	3	7	0	0	
PM12	62	22	7	2	7	0	0	
PM13	56	25	5	1	7	6	0	
PM14	57	28	2	7	6	0	0	
PM15	62	24	6	4	4	0	0	Smectite: 65%, Kaolinite: 25%, Chlorite: 5%, Illite: 5%
PM16	33	12	1	2	4	0	48	

further supported by the range of the silt fraction mean grain size between 14 and 30 μm (Table 1), which is similar to those for modern Sahara dust deposits from Crete, which range 4–8 μm and 16–30 μm

(Goudie & Middleton, 2001; Mattsson & Nihlén, 1996). In terms of Sahara dust provenance fingerprinting, the $^{87}Sr/^{86}Sr$ and ε_{Nd} values of the PM soil samples fall within the range (1σ) of the central North
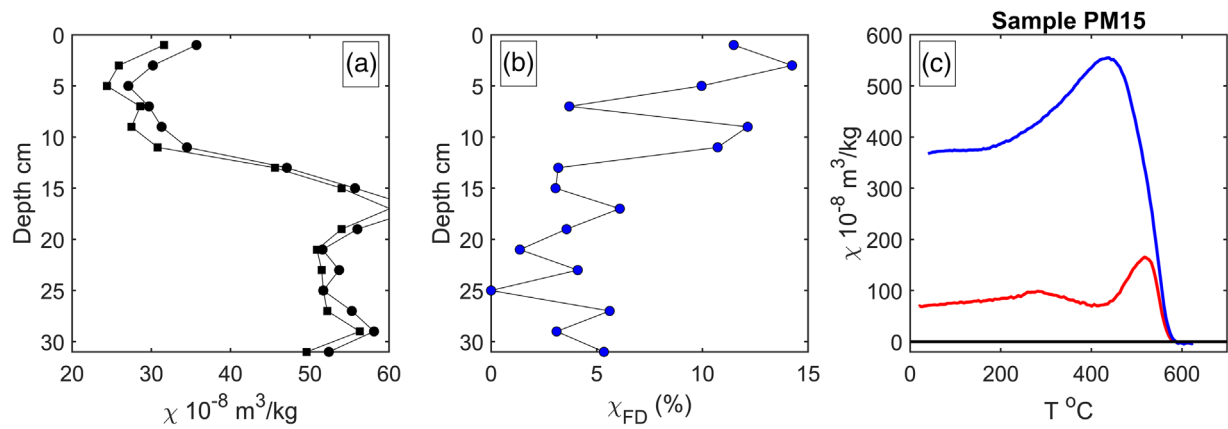
FIGURE 8 Depth variations of low and high frequency (a) and frequency-dependent magnetic susceptibility (b), and thermomagnetic analysis results of sample PM15 (c, red heating curve, blue cooling curve).

TABLE 3 Radiogenic isotope results for the PM soil profile and the 2018 Sahara dust (SD) samples.

Sample ID	$^{87}Sr/^{86}Sr$	$^{87}Sr/^{86}Sr$ Std err (%)	$^{143}Nd/^{144}Nd$	$^{143}Nd/^{144}Nd$ Std. err. (%)	ε_{ND}
NBS 987 Sr standard	0.7102500	0.0008	-	-	
La Jolla Nd standard	-	-	0.5118500	0.0006	
PM1	0.7197322	0.0008	0.5121292	0.0004	−9.77
PM2	0.7201146	0.0026	0.5121383	0.0006	−9.60
PM3	0.7205816	0.0009	0.5121390	0.0006	−9.58
PM4	0.7207105	0.0010	0.5121399	0.0007	−9.56
PM5	0.7206530	0.0029	0.5121278	0.0009	−9.80
PM6	0.7205393	0.0007	0.5121419	0.0005	−9.52
PM7	0.7199828	0.0008	0.5121641	0.0005	−9.09
PM8	0.7196993	0.0009	0.5121731	0.0006	−8.91
PM9	0.7197594	0.0008	0.5121694	0.0005	−8.98
PM10	0.7199571	0.0007	0.5121775	0.0004	−8.82
PM11	0.7199244	0.0009	0.5121869	0.0006	−8.64
PM12	0.7196162	0.0008	0.5121820	0.0006	−8.74
PM13	0.7193930	0.0008	0.5121890	0.0006	−8.60
PM14	0.7194477	0.0009	0.5121694	0.0005	−8.98
PM15	0.7191162	0.0011	0.5121795	0.0004	−8.79
PM16	0.7143748	0.0016	0.5122328	0.0005	−7.75
SD 2018	0.7122721	0.0009	0.5122813	0.0006	−6.80

Note: ε_{ND} values were calculated.

African dust source area, which broadly involves the Bodele depression (PSA2; Jewell et al., 2021).

5 | DISCUSSION

5.1 | PM soil parent material

The mineralogical analyses show that calcite is the dominant mineral phase of MK and TZ interbedded sandy sediment and PM basal layers (Figure 7, lower XRD diagrams TZ01 and Table 2 sample PM 16), which in the periglacial environment of Mount Olympus is expected to dissolve slowly (e.g., Gaillardet et al., 2019) and produce an insoluble residue that comprises the PM soil parent material. MacLeod

(1980) analysed the mineral composition of the insoluble residue of carbonates from western Greece and defined a mineralogical suite of quartz, kaolinite and mica (illite). Kantiranis (2001) studied the carbonate rocks of northwestern Greece and found insoluble residue ~1 wt.% consisting mainly of micas, quartz, hematite, chlorite, feldspars and amphibole, whereas the insoluble residue of carbonate basement rocks from Crete also resembles ~1 wt.% of the whole rock samples and is composed of a sandy loam matrix rich in quartz, plagioclase (albite) and mica (illite) (Kirsten & Heinrich, 2022), in agreement with recent studies in northeast Adriatic coast (Razum et al., 2023). Thus, the dissolution of the local carbonate parent material within the interbedded sediment layers and in the basal layer of PM soil can release very small quantities of bedrock-derived impurities such as quartz, plagioclase, illite and kaolinite that are incorporated in the
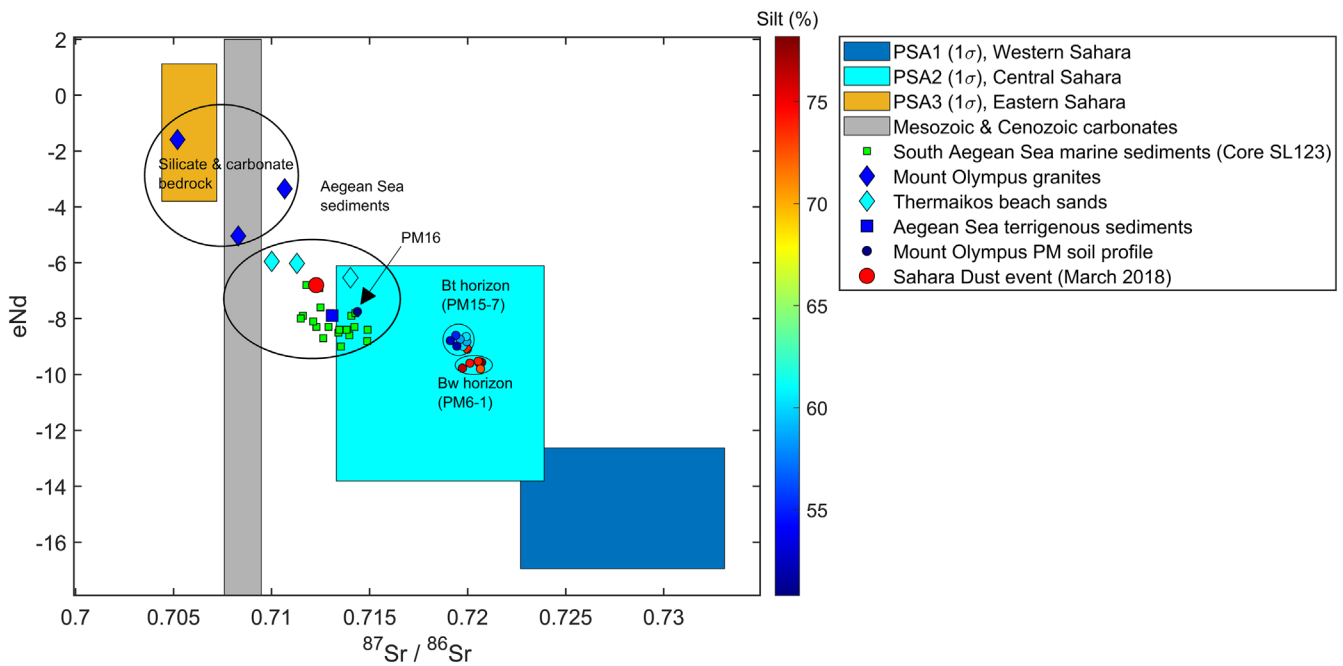
FIGURE 9 Plot of $^{87}Sr/^{86}Sr$ against ε_{ND} values of the PM soil samples, with respective values of Mesozoic and cretaceous carbonates (Frank et al., 2021), Mount Olympus granites (located on the continental west side of the massif (Castorina et al., 2020, Šarić et al., 2009), Aegean Sea terrigenous and coastal sediments (Weldeab et al., 2002) and South Aegean marine sediments from Core SL 123 (Ehrmann et al., 2007), along with the three main North African dust source areas (PSA, Jewell et al., 2021). The isotopic enrichment trend for the PM soil samples towards crustal more radiogenic values occurs with a 25% increase in silt contents (color bar) from the base to the surface of the PM soil profile, suggesting an increasing influence of aeolian dust.

solum but cannot explain the ~30-cm-thick PM soil mantle and ~60-cm thickness of the layers interbedded in the scree slopes.

It has also been proposed that clay in terra rossa soils can derive from isovolumetric replacement of calcite to authigenic clays across a metasomatic front, but this mechanism requires a significant input of aeolian dust to provide essential elements such as Al, Si, Fe and K for clay formation (Merino & Banerjee, 2008). Even though we did not estimate the dissolution rate of Mount Olympus bedrock meta-carbonates and the elemental composition of the insoluble residue, we consider that the fine earth (silt and clay) contents of MK and TZ interbedded layers, which average 10% and 25%, respectively, cannot be derived only by carbonate dissolution and/or by isovolumetric replacement of calcite. Küfmann (2008), Krklec et al. (2022) and Ott et al. (2023) propose carbonate bedrock dissolution rates between ~0.23, 0.15 and 0.4 cm ka^{-1}, respectively, which for the postglacial (12.5 ka BP to present) alpine soil formation on Mount Olympus imply ~5 cm of carbonate loss to soil formation, a value too low to explain the observed thickness of MK and TZ interbedded layers and of the PM soil as a result of residual clay accumulation alone. Our direct observations of episodic Sahara dust deposition on the snowpack of Mount Olympus (Figure 3) provide undisputable evidence of Sahara dust accretion on PM soil. The relative contribution of local dust from moraines, outwash plains and from silicate bedrock formations in the vicinity of Mount Olympus is estimated in the following section, but irrespective of the dust sources (Saharan and/or local), the high-energy erosive regime of Mount Olympus alpine critical zone inter-cepts the formation of extensive aeolian dust mantles, like the one found on the low-energy stable Plateau of Muses. We thus suggest that the production of silt and clay in the PM soil basal layer partly reflects the contribution of mechanically produced sandy and fine

earth carbonate debris and its dissolution products, which together with aeolian dust accretion, comprise the parent materials for the PM soil production.

5.2 | Relative contributions of aeolian dust inputs

Studies on terra rossa soils in Greece, with typical bimodal grain size distributions consisting of clay and silt subpopulations with grain size ranges of 2–4 and 10–40 μm, respectively, ascribe the clay fraction, which is rich in illite and kaolinite, to the limestone residue, and the silt fraction, which is made up entirely of quartz, to long-range aeolian transport from variable sources (Mizota et al., 1988; Runnels & van Andel, 2003). In line with this notion, we considered the quartz wt.% content in the solum, as a proxy for aeolian dust in general and not exclusively of Sahara dust. The rounded shape of quartz grains observed in SEM images (Figure 11d), provides supplementary evidence for their aeolian origin. Furthermore, we consider that the neodymium-derived mass fraction (*f*), is solely a proxy of Sahara dust accretion. This is supported by the high statistical correlation between the silt fraction (M3) with the ε_{ND}-derived *f* fraction ($R^2 = 0.73$, $p < 0.001$) and by the similarity of the grain size ranges between the silt fraction and the modern Sahara dust deposits. The mass fraction (*f*) of Sahara-dust-derived ε_{ND} was calculated based on the highest ε_{Nd} value of sample PM16 and Aegean Sea sediments ($\varepsilon_{Nd} = -5.94$) and on the lowest value of Sahara dust PSA2 ($\varepsilon_{Nd} = -13.81$) end members. The ε_{Nd} value of Aegean Sea sediments is considered conservative in relation to that of Mount Olympus bedrock due to the mixing of the carbonate bedrock sediments with siliciclastic and biogenic sediments during fluvial transport.

The ε_{ND}-based Sahara dust contributions to the PM soil vary between ~35% and ~50% (except that of basal sample PM16) (Figure 10). Conversely, the quartz-derived aeolian dust contribution ranges between ~45% and 65% shows a relatively small variation with depth and an abrupt increase (~25%) from sample PM16 to PM15 (Figure 10). The basal sample PM16 exhibits the lowest contributions of quartz concentration, f ratio values (Figure 10) and silt concentrations (Table 1; Figure 6) and is considered an outlier representing the regolith–soil mix, which agrees with its distinct color and its lowest magnetic susceptibility values. The preservation of quartz in the PM soil profile and especially in the lower Bt horizon requires a mechanism of reduced Sahara dust input and/or loss to weathering, with simultaneous inputs of other quartz-rich-derived dust. A pattern that can explain the lower ε_{Nd}-based Sahara dust contributions in the Bt horizon and the near steady quartz contents is a shift in atmospheric circulation patterns that resulted in less-frequent dust transport episodes from north Africa along with steady aeolian quartz accretion from local quartz sources. Aeolian quartz from the silicate bedrock formations of the Pieria mountains, Mount Olympus granites and even from the Katerini alluvial plane (Figure 1) can be deposited on Mount Olympus periglacial zone during periods of regional aridity, associated with thinning of vegetation, desiccation of the Katerini alluvial plane and immobilization of fine dust grains through convection.

Based on the above, we tentatively attribute the ~15% difference between the ε_{Nd}-based estimates and the quartz-based estimates to the accretion of quartz-rich dust from local sources during the formation of the Bt horizon, considering that the contribution of bedrock-derived quartz from the insoluble residue is ~1%. From the ε_{Nd}-based contributions, we estimate that the Sahara dust accretion to PM soil is between ~35% to 50%, whereas local sources can potentially accrete another ~15%. Our estimated aeolian dust accretion ~65% is similar to the one in the North Calcareous Alps, where the local contribution of dust from the periglacial zone of the North Calcareous and Austrian silicate Alps is significant (Küfmann, 2008), but our estimated Sahara dust contribution in the PM soil is higher than its respective average contribution (20%–30%, Varga et al., 2016) in interglacial soils of the Carpathian Basin. We attribute this difference to the closer proximity of Mount Olympus to the Sahara Desert compared to the Carpathian basin. Given that these values are conservative estimates, the aeolian contribution may potentially be higher as, in our calculations, we have not included aeolian-transported micas and clays that are integral parts of Sahara dust samples deposited on the snowpack. We thus suggest that the aeolian dust accretion comprises a minimum of ~65% of the PM soil parent material and that carbonate bedrock erosion, contribution of bedrock insoluble residue and pedogenetic production of detrital clays can potentially contribute another ~35% to the development of PM soil.

5.3 | Pedogenetic alterations

An alternative mechanism that can explain the nearly homogeneous depth distribution of quartz (Figure 10) is soil mixing by cryoturbation and subsequent translocation of fine earth particles from Bw to Bt horizon. The mechanism of illuviation does not necessarily cancel the climatic forcing of Sahara dust reduction and increase of local dust inputs during the development of the Bt horizon but can act synergistically. For example, a cold and arid climatic phase that immobilises quartz-rich dust from Mount Olympus and Pieria mountains piedmonts can also reactivate the periglacial processes on the Mount Olympus alpine critical zone, which in turn enhances scree slope aggradation, colluvial activity, intensification of freeze–thaw cycles, and cryoturbation of the soils. Cryogenically induced translocation of detrital silt and clay deposited on the surface of the Bw horizon distorts the textural composition and
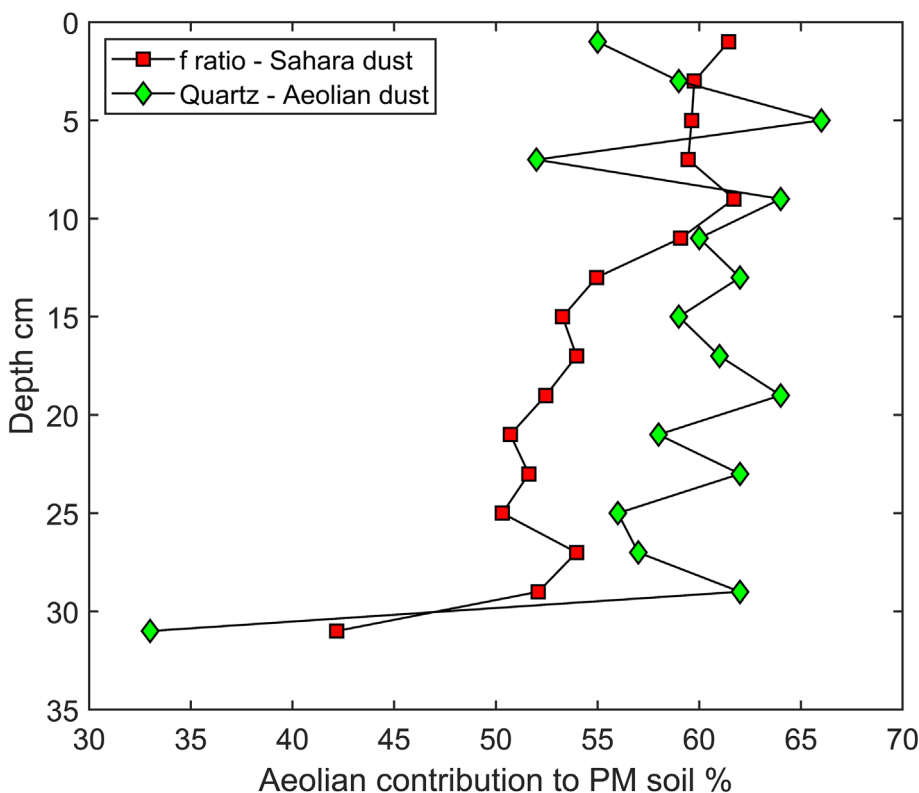
FIGURE 10 Estimates of the relative contributions of aeolian dust accretion to the PM soil as calculated by mineralogical, and isotopic proxies. The ε_{ND} derived f ratio is considered as a proxy of Sahara dust, whereas the quartz (wt.%) of the bulk samples is representative of both local and Saharan dust sources.

soil properties and results in massive structures like the one we observed in the PM soil profile (Figure 4).

Despite the absence of color difference and of distinct layers in the PM soil, the higher magnetic susceptibility values of the Bt compared to the Bw horizon can result from the enrichment of ferromagnetic minerals during in situ weathering of translocated detrital fine earth particles through pedogenesis (Maher, 2011). However, the overall low values of the frequency-dependent magnetic susceptibility (χ_{FD} < 10) in the lower Bw point to low production of magnetic nanoparticles and to weak pedogenetic alteration of the soil (Dearing et al., 1996), which in the base of PM soil profile occurs through the oxidation of ultrafine

(titano)magnetite to maghemite (Section 4.4). The SEM-EDS analyses show the presence of ultrafine Fe–Ti grains throughout the solum (Figure 11b) apart from regolith sample PM16 (Figure 11a). This is further supported by the EDS chemical composition of the calcite grains in basal sample PM16 that have TiO_2 weight % concentration <1%. On the other hand, magnetite is found attached to clay minerals of the Bodélé depression surface sediments (Moskowitz et al., 2016), which is the major source of Sahara dust in PM soil (Figure 10). Also, magnetic susceptibility measurements of Sahara dust modern deposits in SE Bulgaria show a low-frequency magnetic susceptibility value of $\chi_{lf} = 97 \times 10^{-8}$ m^3 kg^{-1} (Jordanova et al., 2013), which is close to the
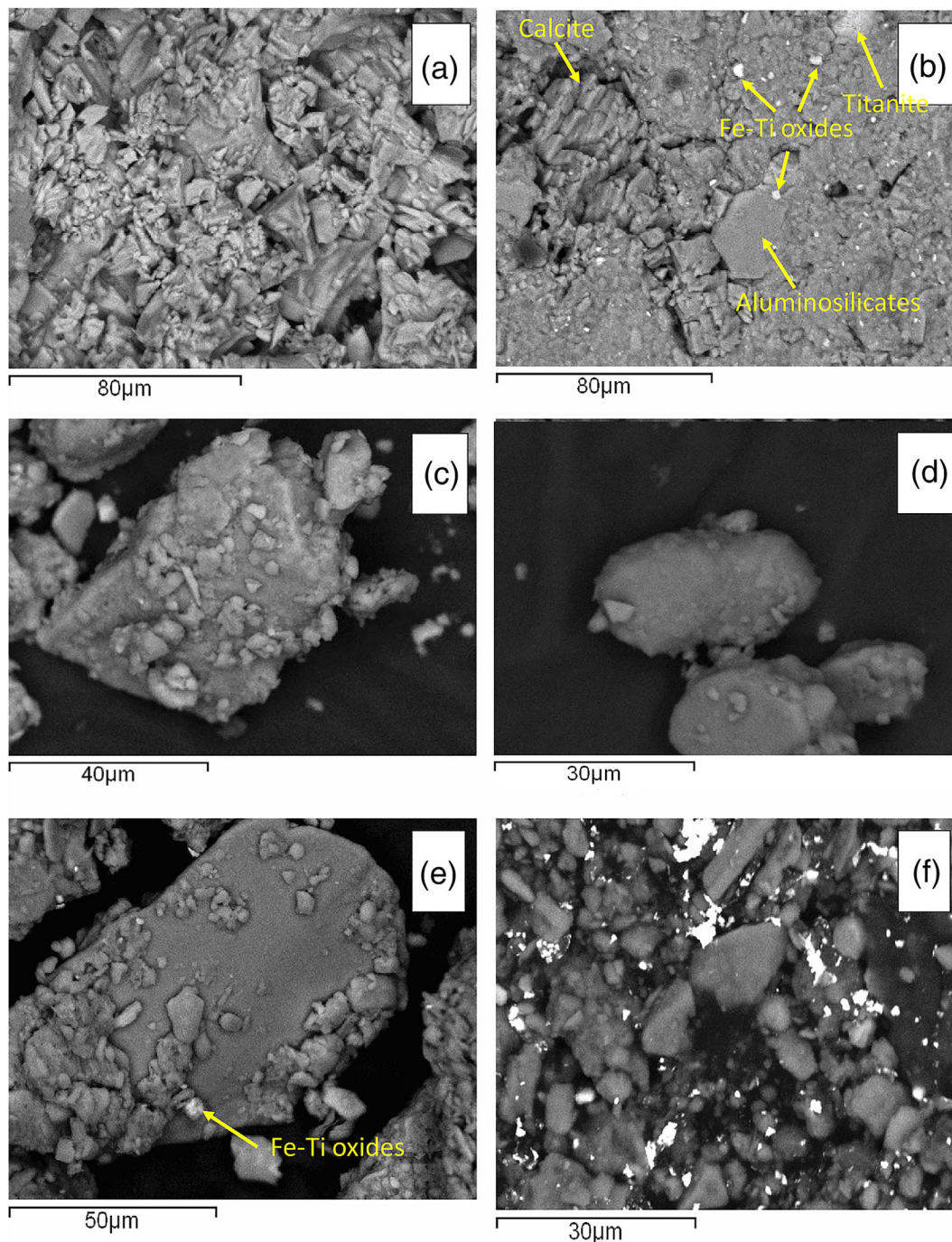

FIGURE 11 SEM backscatter images from selected samples of the PM soil profile. (a) Calcite grains from basal sample PM16. (b) Mixed phase of aluminosilicates with calcite, Fe–Ti oxides (titanomagnetite) and titanite from basal sample PM16. (c) K-feldspar coated with clays. (d) Quartz grain with rounded edges that result from long-range aeolian transport. (e) Surface sample PM1 aggregate of aluminosilicates, clays, and Fe–Ti oxides. (f) Quartz grains of variable shapes and grain sizes from sample PM3 with Fe–Ti oxides.

values of Bw horizon ($\chi_{lf} = 86 \times 10^{-8}$ m^3 kg^{-1}) and Sahara dust episodes are known to transport Fe–Ti oxides in the Mediterranean region (Rodriguez-Navarro et al., 2018). We can therefore ascribe the observed Fe–Ti oxides and (titano)magnetite an aeolian origin, from either the local igneous silicate outcrops or from the Sahara Desert. Collectively, these observations imply that the magnetic enhancement of the Bt compared to the Bw horizon can result from a combination of fine earth illuviation of aeolian-transported ultrafine magnetic particles through cryoturbation and subsequent weak pedogenetic modifications. The latter result in the oxidation of magnetic minerals like (titano)magnetite and can also explain the reddish to yellow color hues.

5.4 | Mineral weathering

In addition to the weak pedogenesis of ferromagnetic minerals in the base of the PM soil profile, we assessed the mineral weathering potential of non-magnetic minerals through the clay mineralogy composition of basal and topsoil samples PM15 and PM1. Both samples show the dominance of smectite with lesser contributions of kaolinite, chlorite and illite (Table 2). High amounts of smectite in alpine soils result from the alteration of detrital chlorite and micas deposited on glacier surfaces and are found in proglacial fields in the European Alps and Rocky Mountains (Egli et al., 2003; Egli et al., 2011; Munroe et al., 2015) so that the 20% difference in smectite concentration (Table 2) between the basal and topsoil layers can be partly related to enhanced mineral chemical weathering in the base of the solum. Similarly, kaolinite observed in the XRD profiles of the MK and TZ and Sahara dust samples (Figure 7) can be released from the dissolution of bedrock carbonates, as are the cases for western Greece (Macleod, 1980) and Crete (Kirsten & Heinrich, 2022) but can also form through the alteration of other detrital minerals, such as plagioclase (albite), a process that is common in glacial and periglacial environments (Anderson et al., 2000). Finally, high smectite and kaolinite contents can also be transported during Saharan dust transport episodes (e.g., Scheuvens et al., 2013), but specifically, they are representative of the western Sahara dust provence (PSA 1, Figure 10; Rodriguez-Navarro et al., 2018). However, smectite and kaolinite are also found in modern Sahara dust samples deposited in Athens, Greece (Remoundaki et al., 2011). Therefore, we consider that the high (>80%) concentration of smectite and kaolinite in the PM soil clay (<2 μm) fraction reflects the balance between direct aeolian deposition and in-situ weathering of detrital (aeolian and/or bedrock derived) micas and plagioclase, but the respective contributions of aeolian-transported versus that of bedrock-derived clay minerals subjected to post-depositional mineral alterations cannot be defined from the existing data.

5.5 | Relative timing of PM soil development

Direct observations suggest that cryoturbation is a fundamental pedogenetic process in the development of PM soil and continues today along with the ongoing accretion of the surficial aeolian silt horizon Bw. The occurrence of seasonal soil freezing and lack of vegetation in the PM polygon centres provide evidence that cryoturbation is active, destroying soil horizonation and obscuring pedogenetic and chemical weathering signals. However, magnetic and mineralogical data indicate the occurrence of weathered Fe-(Ti) oxides such as (titano)

maghemite and the dominance of smectite and kaolinite in the soil basal and topsoil layers, which enable us to conclude that mineral alteration and pedogenetic modifications of deposited aeolian dust and of local erosional products are ongoing processes within the PM soil profile, occurring in tandem with cryoturbation.

In the absence of absolute datings that can constrain temporally the processes driving the production of PM soil, we hypothesised on its age based on the conclusions drawn from the contributions of aeolian dust and the impacts of cryoturbation. We tentatively ascribe the deposition of the base colluvial layer and/or the in-situ fragmentation of the regolith's till boulders to the most recent period of glacial activity on Mount Olympus. Based on the glacial record of the MK and TZ cirques (Section 2.1), the best candidates of periglacial activity that have likely resulted in the deposition of outwash sand and gravels postdate the moraine stabilization phases at ~12.5, 2.5 and 0.6 ka BP.

However, there is a 10-ka time span between the Holocene–Pleistocene boundary and the late-Holocene glacial expansions on Mount Olympus. Accepting that PM soil formation began after the moraine stabilization phase at ~12.5 ka BP that was common to MK and TZ cirques, its production rate would be ~3 $\times 10^{-5}$ m year^{-1} assuming that soil erosion in the low-lying PM has been minimal. This rate is considerably lower than the respective soil production rates of Alpine and Mediterranean soils formed over the last 10 ka (Egli et al., 2018; Figure 8). In contrast, by considering a late-Holocene age and that the PM soil development postdates the ~2.5 ka BP moraine stabilization phase, the soil production rate is ~1 $\times 10^{-4}$ m year^{-1} an estimate that is in better agreement with the soil production rates presented by Egli et al. (2018) for both Alpine and Mediterranean soils. Furthermore, a late-Holocene development of PM soil broadly agrees with soil development patterns in diverse geomorphological environments in Crete (Kirsten & Heinrich, 2022). If this scenario is correct, then we can further hypothesise that the development of the Bt horizon could have lasted between ~2.5 and 1.0 ka BP, before a recorded phase of intense Sahara dust accretion in the Mediterranean that resulted from the combined action of an orbitally induced decrease in solar insolation and increased aridity over North Africa (Sabatier et al., 2020). This shift could potentially explain the sharp textural boundary between the Bt and Bw horizons and the increasing Sahara dust accretion on the upper Bw horizon. The hypothesised development of the Bw horizon over the past 1 ka could have been disturbed by cryoturbation during the LIA (~0.6 ka BP) glacial expansion in the MK and that continues until today. Ongoing work on Mount Olympus alpine critical zone involves efforts to accurately date the MK and TZ scree interbedded layers and the PM soil profile through optically stimulated luminescence dating that is aided by the high concentrations of quartz in the fine earth fraction, as well as additional geochemical analysis and estimates of the local carbonate bedrock dissolution rates and its residual geochemical composition, in an overall attempt to provide a new continuous record of postglacial alpine landscape evolution in the Mediterranean periglacial zone.

6 | CONCLUSIONS

In this study, we investigated the local processes that lead to the development of alpine soil profile on a stable landform on Mount Olympus, considering its regional setting representative of Mediterranean

carbonate mountains that became gradually ice-free during the Pleistocene–Holocene transition, but that have also been affected by late-Holocene climatic shifts towards glacial and periglacial conditions (Oliva et al., 2018). We discussed the relative contributions of erosion, aeolian dust accretion, post-depositional pedogenesis, and mineral alteration by comparing colluvial sediment layers interbedded in scree slopes with a soil B horizon developed on a regolith composed of slope outwash deposits and fragmented till boulders along a 2-km hillslope energy gradient with a northeasterly orientation, which is the main direction of glacial cirque development on Mount Olympus.

Overall, our results suggest that soils developed in stable landforms like the PM show signs of weak pedogenesis and contain higher amounts of aeolian dust than locally eroded and chemically weathered products. Aeolian dust from local and Saharan sources is accreted in alpine soils formed in periglacial hummocky polygons of the PM and comprises ~30%–65% of the soil mass weight. This interpretation matches those of several other studies on aeolian dust accretion in alpine soils (e.g., Gild et al., 2018; Kirsten & Heinrich, 2022; Küfmann, 2008; Munroe et al., 2015; Yang et al., 2016) and suggests that aeolian dust is the primary parent soil material on Mount Olympus. The major source of Sahara dust deposited on Mount Olympus is the Bodélé depression, which agrees with observations of accreted dust in Crete (Pye, 1992).

In the low-erosional environment of the PM, mineral alteration and weak pedogenetic modifications occur throughout the solum, but their signal is blurred by soil mixing due to cryoturbation. A sharp textural boundary not visible in the field separates an upper weathered soil Bw horizon from the lower illuvial Bt horizon, which is magnetically enhanced and enriched in smectite and kaolinite. Radiogenic isotope systematics, mineralogy and magnetic susceptibility value range classify the Bw horizon as an aeolian silt layer that was likely formed during a late-Holocene shift of regional atmospheric circulation that resulted in increased Sahara dust accretion in Mediterranean alpine landscapes.

AUTHOR CONTRIBUTIONS

Michael Styllas conceptualised the study and the methodology. Michael Styllas, Christos Pennos, Aurel Persoiu and Athanasios Godelitsas realised the fieldwork and sampling campaigns. Michael Styllas, Christos Pennos, Matthieu Ghilardi, Francois Demory, Mihai N. Ducea, Lambrini Papadopoulou, Elina Aidona and Nikolaos Kantiranis conducted the laboratory analyses. Aurel Persoiu and Athanasios Godelitsas supervised the broader context of the study. Michael Styllas wrote the manuscript with input from all co-authors.
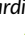
CONFLICT OF INTEREST STATEMENT

The authors declare no conflict of interest.

DATA AVAILABILITY STATEMENT

The data that support the findings of this study are available from the corresponding author upon reasonable request.

ORCID

Michael Styllas https://orcid.org/0000-0003-4385-0008
Christos Pennos https://orcid.org/0000-0001-9722-2766
Aurel Persoiu https://orcid.org/0000-0001-9506-0070
Athanasios Godelitsas https://orcid.org/0000-0003-2676-2612
Lambrini Papadopoulou https://orcid.org/0000-0002-4643-9364
Elina Aidona https://orcid.org/0000-0002-1974-9105
Nikolaos Kantiranis https://orcid.org/0000-0001-7874-4219
Mihai N. Ducea https://orcid.org/0000-0002-5322-0782
Matthieu Ghilardi https://orcid.org/0000-0003-2709-1769
Francois Demory https://orcid.org/0000-0002-7526-9886

REFERENCES

Allard, J.L., Hughes, P.D., Woodward, J.C., Fink, D., Simon, K. & Wilcken, K.M. (2020) Late Pleistocene glaciers in Greece: a new ^{36}Cl chronology. *Quaternary Science Reviews*, 245, 106528. Available from: https://doi.org/10.1016/j.quascirev.2020.106528

Amit, R., Enzel, Y. & Crouvi, O. (2020) Quaternary influx of proximal coarse-grained dust altered circum-Mediterranean soil productivity and impacted early human culture. *Geology*, 49(1), 61–65. Available from: https://doi.org/10.1130/G47708.1

Anderson, S.P., Drever, J.I., Frost, C.D. & Holden, P. (2000) Chemical weathering in the foreland of a retreating glacier. *Geochimica et Cosmochimica Acta*, 64(7), 1173–1189. Available from: https://doi.org/10.1016/S0016-7037(99)00358-0

Capo, R.C., Stewart, B.W. & Chadwick, O.A. (1998) Strontium isotopes as tracers of ecosystem processes: theory and methods. *Geoderma*, 82(1-3), 197–225. Available from: https://doi.org/10.1016/S0016-7061(97)00102-X

Castorina, F., Magganas, A., Masi, U. & Kyriakopoulos, K. (2020) Geochemical and Sr-Nd isotopic evidence for petrogenesis and geodynamic setting of Lower-Middle Triassic volcanogenic rocks from Central Greece: implications for the Neotethyan Pindos Ocean. *Mineralogy and Petrology*, 114(1), 39–56. Available from: https://doi.org/10.1007/s00710-019-00687-7

Conroy, J.L., Overpeck, J.T., Cole, J.E., Liu, K.B., Wang, D. & Ducea, M.D. (2013) Dust and temperature influences on glaciofluvial sediment deposition in southwestern Tibet during the last millennium. *Global and Planetary Change*, 107, 132–144. Available from: https://doi.org/10.1016/j.gloplacha.2013.04.009

D'Amico, M.E., Casati, E., Abu El Khair, D., Cavallo, A., Barcella, M. & Previtali, F. (2023) Aeolian inputs and dolostone dissolution involved in soil formation in Alpine karst landscapes (Corna Bianca, Italian Alps). *Catena*, 230, 107254. Available from: https://doi.org/10.1016/j.catena.2023.107254

Dearing, J., Hay, K., Baban, S., Huddleston, A., Wellington, E. & Loveland, P. (1996) Magnetic susceptibility of soil: an evaluation of conflicting theories using a national data set. *Geophysical Journal International*, 127(3), 728–734. Available from: https://doi.org/10.1111/j.1365-246X.1996.tb04051.x

Dobiński, W. (2005) Permafrost of the Carpathian and Balkan Mountains, Eastern and Southeastern Europe. *Permafrost and Periglacial Processes*, 16(4), 395–398. Available from: https://doi.org/10.1002/ppp.524

Drewnik, M., Skiba, M., Szymański, W. & Żyla, M. (2014) Mineral composition vs. soil forming processes in loess soils—a case study from Kraków (Southern Poland). *Catena*, 119, 166–173. Available from: https://doi.org/10.1016/j.catena.2014.02.012

Ducea, M.N., Barla, A., Stoica, A.M., Panaiotu, C. & Petrescu, L. (2020) Temporal-geochemical evolution of the Persani volcanic field, eastern Transylvanian Basin (Romania): implications for slab rollback beneath the SE Carpathians. *Tectonics*, (39), e2019TC005802. Available from: https://doi.org/10.1029/2019TC005802

Dunlop, D.J. & Özdemir, Ö. (1997) *Rock magnetism: fundamentals and frontiers*. Cambridge, New York: Cambridge University Press.

Durn, G. (2003) Terra rossa in the Mediterranean region: parent materials, composition and origin. *Geologika Croatia*, 56(1), 83–100. Available from: https://doi.org/10.4154/GC.2003.06

Durn, G., Ottner, F. & Slovenec, D. (1999) Mineralogical and geochemical indicators of the polygenetic nature of terra rossa in Istria, Croatia. *Geoderma*, 91(1-2), 125–150. Available from: https://doi.org/10.1016/S0016-7061(98)00130-X

Egli, M., Dahms, D. & Norton, K. (2014) Soil formation rates on silicate parent material in alpine environments: different approaches–different results? *Geoderma*, 213, 320–333. Available from: https://doi.org/10.1016/j.geoderma.2013.08.016

Egli, M., Hunt, A.G., Dahms, D., Raab, G., Derungs, C., Raimondi, S., et al. (2018) Prediction of soil formation as a function of age using the percolation theory approach. *Frontiers in environmental. Science*, 6, 108. Available from: https://doi.org/10.3389/fenvs.2018.00108

Egli, M., Mirabella, A. & Fitze, P. (2003) Formation rates of smectites derived from two Holocene chronosequences in the Swiss Alps. *Geoderma*, 117(1-2), 81–98. Available from: https://doi.org/10.1016/S0016-7061(03)00136-8

Egli, M. & Poulenard, J. (2016) Soils of mountainous landscapes. In: Richardson, D., Castree, N., Goodchild, M.F., Kobayashi, A., Liu, W. & Marston, R.A. (Eds.) *International encyclopedia of geography: people, the earth, environment and technology*. John Wiley & Sons, Ltd. https://doi.org/10.1002/9781118786352.wbieg0197

Egli, M., Wernli, M., Burga, C., Kneisel, C., Mavris, C., Valboa, G., et al. (2011) Fast but spatially scattered smectite-formation in the proglacial area Morteratsch: an evaluation using GIS. *Geoderma*, 164(1-2), 11–21. Available from: https://doi.org/10.1016/j.geoderma.2011.05.001

Ehrmann, W., Schmiedl, G., Hamann, Y., Kuhnt, T., Hemleben, C. & Siebel, W. (2007) Clay minerals in late glacial and Holocene sediments of the northern and southern Aegean Sea. *Palaeogeography, Palaeoclimatology, Palaeoecology*, 249(1–2), 36–57. Available from: https://doi.org/10.1016/j.palaeo.2007.01.004

Erel, Y. & Torrent, J. (2010) Contribution of Saharan dust to Mediterranean soils assessed by sequential extraction and Pb and Sr isotopes. *Chemical Geology*, 275(1-2), 19–25. Available from: https://doi.org/10.1016/j.chemgeo.2010.04.007

Frank, A.B., Frei, R., Triantaphyllou, M., Vassilakis, E., Kristiansen, K. & Frei, K.M. (2021) Isotopic range of bioavailable strontium on the Peloponnese peninsula, Greece: a multi-proxy approach. *Science of the Total Environment*, 774, 145181. Available from: https://doi.org/10.1016/j.scitotenv.2021.145181

Gaillardet, J., Calmels, D., Romero-Mujalli, G., Zakharova, E. & Hartmann, J. (2019) Global climate control on carbonate weathering intensity. *Chemical Geology*, 527, 118762. Available from: https://doi.org/10.1016/j.chemgeo.2018.05.009

Garzanti, E., Andò, S. & Vezzoli, G. (2009) Grain-size dependence of sediment composition and environmental bias in provenance studies. *Earth and Planetary Science Letters*, 277(3–4), 422–432. Available from: https://doi.org/10.1016/j.epsl.2008.11.007

Gild, C., Geitner, C. & Sanders, D. (2018) Discovery of a landscape-wide drape of late-glacial aeolian silt in the western Northern Calcareous Alps (Austria): first results and implications. *Geomorphology*, 301, 39–52. Available from: https://doi.org/10.1016/j.geomorph.2017.10.025

Goudie, A.S. & Middleton, N.J. (2001) Saharan dust storms: nature and consequences. *Earth Science Reviews*, 56(1-4), 179–204. Available from: https://doi.org/10.1016/S0012-8252(01)00067-8

Grousset, F.E. & Biscaye, P.E. (2005) Tracing dust sources and transport patterns using Sr, Nd and Pb isotopes. *Chemical Geology*, 222(3-4), 149–167. Available from: https://doi.org/10.1016/j.chemgeo.2005.05.006

Haeberli, W., Hallet, B., Arenson, L., Elconin, R., Humlum, O., Kääb, A., et al. (2006) Permafrost creep and rock glacier dynamics. *Permafrost and Periglacial Processes*, 17(3), 189–214. Available from: https://doi.org/10.1002/ppp.561

Jewell, A.M., Drake, N., Crocker, A.J., Bakker, N.L., Kunkelova, T., Bristow, C.S., et al. (2021) Three North African dust source areas and

their geochemical fingerprint. *Earth and Planetary Science Letters*, 554, 116645. Available from: https://doi.org/10.1016/j.epsl.2020.116645

Jordanova, D., Georgieva, B., Jordanova, N., Guyodo, Y. & Lagroix, F. (2022) Holocene palaeoenvironmental conditions in NE Bulgaria uncovered by mineral magnetic and paleomagnetic records of an alluvial soil. *Quaternary International*, 631, 47–58. Available from: https://doi.org/10.1016/j.quaint.2022.06.009

Jordanova, N., Jordanova, D., Qingsong, L., Pengxiang, H., Petrov, P. & Petrovský, E. (2013) Soil formation and mineralogy of a Rhodic Luvisol—insights from magnetic and geochemical studies. *Global and Planetary Change*, 110, 397–413. Available from: https://doi.org/10.1016/j.gloplacha.2013.08.020

Kantiranis, N. (2001) *Calcination study of the crystalline limestone from Agios Panteleimonas, Florina, Greece*. PhD Thesis. Thessaloniki, Greece: School of Geology, Aristotle University of Thessaloniki 196p.

Kirsten, F. & Heinrich, J. (2022) Soil-sediment-configurations on slopes of Central and Western Crete (Greece) and their implications for late Holocene morphodynamics and pedogenesis—a conceptual approach. *Catena*, 214, 106238, 0341-8162. Available from: https://doi.org/10.1016/j.catena.2022.106238

Krklec, K., Braucher, R., Perica, D. & Domínguez-Villar, D. (2022) Long-term denudation rate of karstic North Dalmatian Plain (Croatia) calculated from ^{36}Cl cosmogenic nuclides. *Geomorphology*, 413, 108358. Available from: https://doi.org/10.1016/j.geomorph.2022.108358

Küfmann, C. (2008) Are cambisols in alpine karst autochthonous or eolian in origin? *Arctic Antarctic and Alpine Research*, 40(3), 506–518. Available from: https://doi.org/10.1657/1523-0430(06-091)[KUEFMANN]2.0.CO;2

Kuhlemann, J., Rohling, E., Krumrei, I., Kubik, P., Ivy-Ochs, S. & Kucera, M. (2008) Regional synthesis of Mediterranean atmospheric circulation during the last glacial maximum. *Science*, 321(5894), 1338–1340. Available from: https://doi.org/10.1126/science.1157638

Kurtz, A.C., Derry, L.A. & Chadwick, O.A. (2001) Accretion of Asian dust to Hawaiian soils; isotopic, elemental, and mineral mass balances. *Geochimica et Cosmochimica Acta*, 65(12), 1971–1983. Available from: https://doi.org/10.1016/S0016-7037(01)00575-0

Lawrence, C.R., Reynolds, R.L., Ketterer, M.E. & Neff, J.C. (2013) Aeolian controls of soil geochemistry and weathering fluxes in high-elevation ecosystems of the Rocky Mountains, Colorado. *Geochimica et Cosmochimica Acta*, 107, 27–46. Available from: https://doi.org/10.1016/j.gca.2012.12.023

Lehmkuhl, F., Nett, J.J., Pötter, S., Schulte, P., Sprafke, T., Jary, Z., et al. (2020) Loess landscapes of Europe—mapping, geomorphology, and zonal differentiation. *Earth Science Reviews*, 215, 103496. Available from: https://doi.org/10.1016/j.earscirev.2020.103496

Lutterotti, L., Bortolotti, M., Ischia, G., Lonardelli, I. & Wenk, H.R. (2007) Rietvelt texture analysis from diffraction images. *Zeitschrift für Kristallographie*, 26(suppl_26), 125–130. Available from: https://doi.org/10.1524/zksu.2007.2007.suppl_26.125

Macleod, D.A. (1980) The origin of the red Mediterranean soils in Epirus, Greece. *European Journal of Soil Science*, 31(1), 125–136. Available from: https://doi.org/10.1111/j.1365-2389.1980.tb02070.x

Maher, B.A. (2011) The magnetic properties of Quaternary aeolian dusts and sediments, and their palaeoclimatic significance. *Aeolian Research*, 3(2), 87–144. Available from: https://doi.org/10.1016/j.aeolia.2011.01.005

Marmureanu, L., Marin, C.A., Andrei, S., Antonescu, B., Ene, D., Boldeanu, M., et al. (2019) Orange snow: a Saharan dust intrusion over Romania during winter conditions. *Remote Sensing*, 11(21), 2466. Available from: https://doi.org/10.3390/rs11212466

Mattsson, J.O. & Nihlén, T. (1996) The transport of Saharan dust to southern Europe: a scenario. *Journal of Arid Environments*, 32(2), 111–119. Available from: https://doi.org/10.1006/jare.1996.0011

Merino, E. & Banerjee, A. (2008) Terra rossa genesis, implications for karst, and eolian dust: a geodynamic thread. *Journal of Geology*, 116(1), 62–75. Available from: https://doi.org/10.1086/524675

Mizota, C., Kusakabe, M. & Noto, M. (1988) Eolian contribution to soil development on Cretaceous limestones in Greece as evidenced by oxygen isotope composition of quartz. *Geochemical Journal*, 22(1), 41–46. Available from: https://doi.org/10.2343/geochemj.22.41

Moskowitz, B.M., Reynolds, R.L., Goldstein, H.L., Berquó, T.S., Kokaly, R.F. & Bristow, C.S. (2016) Iron oxide minerals in dust-source sediments from the Bodélé Depression, Chad: implications for radiative properties and Fe bioavailability of dust plumes from the Sahara. *Aeolian Research*, 22, 93–106. Available from: https://doi.org/10.1016/j.aeolia.2016.07.001

Muhs, D.R. & Benedict, J.B. (2006) Eolian additions to late Quaternary alpine soils, Indian Peaks Wilderness area, Colorado Front Range. *Arctic Antarctic and Alpine Research*, 38(1), 120–130. Available from: https://doi.org/10.1657/1523-0430(2006)038[0120:EATLQA]2.0.CO;2

Munroe, J.S., Attwood, E.C., O'Keefe, S.S. & Quackenbush, P.J. (2015) Eolian deposition in the alpine zone of the Uinta Mountains, Utah, USA. *Catena*, 124, 119–129. Available from: https://doi.org/10.1016/j.catena.2014.09.008

Munroe, J.S., Norris, E.D., Carling, G.T., Beard, B.L., Satkoski, A.M. & Liu, L. (2019) Isotope fingerprinting reveals western North American sources of modern dust in the Uinta Mountains, Utah, USA. *Aeolian Research*, 38, 39–47. Available from: https://doi.org/10.1016/j.aeolia.2019.03.005

Oliva, M., Žebre, M., Guglielmin, M., Hughes, P.D., Çiner, A., Vieira, G., et al. (2018) Permafrost conditions in the Mediterranean region since the Last Glaciation. *Earth Science Reviews*, 185, 397–436. Available from: https://doi.org/10.1016/j.earscirev.2018.06.018

Ott, R. F., Gallen, S. F. & Helman, D. (2023) Erosion and weathering in carbonate regions reveal climatic and tectonic drivers of carbonate landscape evolution. *Earth Surface Dynamics*, 11, 247–257. Available from: https://doi.org/10.5194/esurf-11-247-2023

Pye, K. (1992) Aeolian dust transport and deposition over Crete and adjacent parts of the Mediterranean Sea. *Earth Surface Processes and Landforms*, 17(3), 271–288. Available from: https://doi.org/10.1002/esp.3290170306

Razum, I., Rubinić, V., Miko, S., Ružičić, S. & Durn, G. (2023) Coherent provenance analysis of terra rossa from the northern Adriatic based on heavy mineral assemblages reveals the emerged Adriatic shelf as the main recurring source of siliciclastic material for their formation. *Catena*, 226, 107083. Available from: https://doi.org/10.1016/j.catena.2023.107083

Rellini, I., Trombino, L., Firpo, M. & Rossi, P.M. (2009) Extending westward the loess basin between the Alps and the Mediterranean region: micromorphological and mineralogical evidence from the northern scope of the Ligurian Alps, Northern Italy. *Geografia Fisica e Dinamica Quaternaria*, 32, 103–116.

Remoundaki, E., Bourliva, A., Kokkalis, P., Mamouri, R.E., Papayannis, A., Grigoratos, T., et al. (2011) PM10 composition during an intense Saharan dust transport event over Athens (Greece). *Science of the Total Environment*, 409(20), 4361-4372. Available from: https://doi.org/10.1016/j.scitotenv.2011.06.026

Rodriguez-Navarro, C., di Lorenzo, F. & Elert, K. (2018) Mineralogy and physicochemical features of Saharan dust wet deposited in the Iberian Peninsula during an extreme red rain event. *Atmospheric Chemistry and Physics*, 18(13), 10089–10122. Available from: https://doi.org/10.5194/acp-18-10089-2018

Runnels, C. & van Andel, T.J. (2003) The early stone age of the nomos of Preveza: landscape and settlement. In: Wiseman, J. & Zachos, K. (Eds.) *Landscape archaeology in Southern Epirus, Greece*, Vol. I, 32. Hesperia Supplement. Athens, Greece: The American School of Classical Studies at Athens, pp. 13–47. Available from: https://doi.org/10.2307/1354046

Sabatier, P., Nicolle, M., Piot, C., Colin, C., Debret, M., Swingedouw, D., et al. (2020) Past African dust inputs in the western Mediterranean area controlled by the complex interaction between the intertropical convergence zone, the North Atlantic Oscillation, and total solar irradiance. *Climate of the Past*, 16(1), 283–298. Available from: https://doi.org/10.5194/cp-16-283-2020

Sanders, D., Ostermann, M. & Kramers, J. (2010) Meteoric diagenesis of Quaternary carbonate rocky talus slope successions (Northern Calcareous Alps, Austria). *Facies*, 56(1), 27–46. Available from: https://doi.org/10.1007/s10347-009-0194-4

Šarić, K., Cvetković, V., Romer, R.L., Christofides, G. & Koroneos, A. (2009) Granitoids associated with East Vardar ophiolites (Serbia, F.Y.R. of Macedonia and northern Greece): origin, evolution and geodynamic significance inferred from major and trace element data and Sr–Nd–Pb isotopes. *Lithos*, 108(1-4), 131–150. Available from: https://doi.org/10.1016/j.lithos.2008.06.001

Scheuvens, D., Schütz, L., Kandler, K., Ebert, M. & Weinbruch, S. (2013) Bulk composition of northern African dust and its source sediments—a compilation. *Earth Science Reviews*, 116, 170–194. Available from: https://doi.org/10.1016/j.earscirev.2012.08.005

Shalev, N., Lazar, B., Halicz, L., Stein, M., Gavrieli, I., Sandler, A., et al. (2013) Strontium isotope fractionation in soils and pedogenic processes. *Procedia Earth and Planetary Science*, 7, 790–793. Available from: https://doi.org/10.1016/j.proeps.2013.03.074

Statham, I. (1976) A scree slope rockfall model. *Earth Surface Processes*, 1(1), 43–62. Available from: https://doi.org/10.1002/esp.3290010106

Stuut, J.B., Smalley, I. & O'Hara-Dhand, K. (2009) Aeolian dust in Europe: African sources and European deposits. *Quaternary International*, 198(1–2), 234–245. Available from: https://doi.org/10.1016/j.quaint.2008.10.007

Styllas, M. (2020) Tracing a late Holocene glacial climatic signal from source to sink under intensifying human erosion of eastern Mediterranean landscapes. *Mediterranean Geoscience Reviews*, 2(1), 91–101. Available from: https://doi.org/10.1007/s42990-020-00031-8)

Styllas, M.N. & Kaskaoutis, D.G. (2018) Relationship between winter orographic precipitation with synoptic and large-scale atmospheric circulation: the case of Mount Olympus, Greece. *Bulletin of the Geological Society of Greece*, 52(1), 45–70. Available from: https://doi.org/10.12681/bgsg.14363

Styllas, M.N., Schimmelpfennig, I., Benedetti, L., Ghilardi, M., Aumaître, G., Bourlès, D., et al. (2018) Late-glacial and Holocene history of the Northeast Mediterranean mountain glaciers—new insights from in situ-produced ^{36}Clbased cosmic ray exposure dating of paleo-glacier deposits on Mount Olympus, Greece. *Quaternary Science Reviews*, 193, 244–265. Available from: https://doi.org/10.1016/j.quascirev.2018.06.020,2018

Styllas, M.N., Schimmelpfennig, I., Ghilardi, M. & Benedetti, L. (2016) Geomorphologic and paleoclimatic evidence of Holocene glaciation on Mount Olympus, Greece. *The Holocene*, 26(5), 709–721. Available from: https://doi.org/10.1177/0959683615618259

Varga, G., Cserhati, C., Kovacs, J. & Szalai, Z. (2016) Saharan dust deposition in the Carpathian Basin and its possible effects on interglacial soil formation. *Aeolian Research*, 22, 1–12. Available from: https://doi.org/10.1016/j.aeolia.2016.05.004

Weldeab, S., Emeis, K.-C., Hemleben, C. & Siebel, W. (2002) Provenance of lithogenic surface sediments and pathways of riverine suspended matter in the Eastern Mediterranean Sea: evidence from 143Nd/144Nd and 87Sr/86Sr ratios. *Chemical Geology*, 186(1–2), 139–149. Available from: https://doi.org/10.1016/S0009-2541(01)00415-6

Wu, L., Krijgsman, W., Liu, J., Li, C., Wang, R. & Xiao, W. (2020) CFLab: a MATLAB GUI program for decomposing sediment grain size distribution using Weibull functions. *Sedimentary Geology*, 398, 105590. Available from: https://doi.org/10.1016/j.sedgeo.2020.105590

Yaalon, D.H. (1997) Soils in the Mediterranean region: what makes them different? *Catena*, 28(3-4), 157–169. Available from: https://doi.org/10.1016/S0341-8162(96)00035-5

Yang, F., Zhang, G.L., Yang, F. & Yang, R.M. (2016) Pedogenetic interpretations of particle-size distribution curves for an alpine environment. *Geoderma*, 282, 9–15. Available from: https://doi.org/10.1016/j.geoderma.2016.07.003